Case Studies in Thermal Engineering 62 (2024) 105122

Contents lists available at ScienceDirect

Case Studies in Thermal Engineering

journal homepage: www.elsevier.com/locate/csite

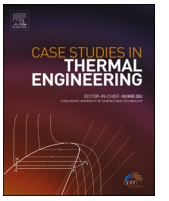

Experimental investigation into thermal characteristics of subcooled flow boiling in horizontal concentric annuli for cooling ultra-fast electric vehicle charging cables

Haein Jung, Seunghyun Lee *

Two-Phase Flow and Thermal Management Laboratory, School of Mechanical Engineering, Gwangju Institute of Science and Technology, 123 Cheomdangwagi-ro, Buk-gu, Gwangju, 61005, South Korea

HIGHLIGHTS

- Subcooled flow boiling is utilized in the cooling system of ultra-fast electric vehicle (EV) charging cables.
- Experiments were conducted to collect data on subcooled boiling in horizontal concentric annuli using HFE-7100.
- Flow visualization shows how thermal boundary layer and flow regime transitions affect heat transfer and critical heat flux.
- Previous correlations were assessed for accuracy in predicting heat transfer coefficients and critical heat flux.
- A 100-kWh electric vehicle can be charged for up to 1.6 min without reaching critical heat flux.

ARTICLE INFO

Keywords:
Subcooled flow boiling
Flow regime transition
Critical heat flux
Concentric annuli
Electric vehicle charging cable
Thermal management

ABSTRACT

In an effort to reduce the charging time of electric vehicles (EVs), the thermal management of the charging system has emerged as one of the most urgent issues. The charging rate has been restricted to avoid thermal failure especially in charging cable. Recently, a direct contact cooling technique that utilizes subcooled flow boiling for charging cables has been proposed and has shown promising thermal management performance. However, there has been a lack of clear explanation regarding its thermal characteristics due to its intrinsically complicated flow features. This study investigates the thermal characteristics of subcooled flow boiling in a horizontally aligned concentric annular tube intended to simulate the direct contact cooling technique employed for charging cables. For the experimental investigation, the wall temperature measurements and high-speed flow visualization images acquired from the transparent test module annulus, with inner and outer diameters of 6.35 mm and 22.0 mm, were utilized. Three key axial thermal characteristics of subcooled flow boiling in annulus have been analyzed, and they are flow regime transition, variation of heat transfer mechanisms, and occurrence of critical heat flux (CHF). The transition of flow regimes and the variation of dominant heat transfer mechanisms in the axial direction are mutually influencing due to the coupled effects between the hydrodynamic and thermal characteristics of simultaneously developing flows. The flow regime changes from partially developed boiling (PDB) to fully developed boiling (FDB) as the intensities of nucleate boiling and bubble recondensation vary in the axial direction, while the dominant heat transfer mechanism shifts from single-phase convection to nucleate boiling, corresponding to the flow regime transition from PDB to FDB. The departure from nucleate boiling (DNB) type CHF is observed, manifested by the wavy interface propagating from the far downstream to the upstream

* Corresponding author.
E-mail address: lees@gist.ac.kr (S. Lee).
URL: https://tpftml.gist.ac.kr/tpftml/index.do (S. Lee).

https://doi.org/10.1016/j.csite.2024.105122
Received 19 June 2024; Received in revised form 26 August 2024; Accepted 12 September 2024
Available online 18 September 2024

region, and the intensities of nucleate boiling and bubble recondensation are also identified as the dominant parameters in determining the occurrence of CHF. Charging time estimation reveals that the proposed method can achieve an 80 % charge for 100-kWh EV batteries in 98 s, while maintaining the cable wire temperature below the safety limit of 80 °C. This strongly supports its potential as a promising thermal management technique for future ultra-fast charging systems.

Nomenclature

A_{ch}	cross-sectional area of the concentric annuli
$A_{ch,i}$	cross-sectional area of the charging cable
A_H	heated surface area of the charging cable
Bo	boiling number, $Bo = q''/Gh_{fg}$
b	empirical coefficient
C	empirical coefficient
c	empirical coefficient
c_p	specific heat at constant pressure
D	diameter
D_h	hydraulic diameter
D_i	charging cable diameter
D_l	laminar equivalent diameter
D_o	inner diameter of the polycarbonate tube
E	enhancement factor
e	exponential function
F	empirical coefficient
Fr	Froude number
G	mass flux
g	gravitational acceleration
h	enthalpy; heat transfer coefficient
h_{fg}	latent heat of vaporization
I_{wire}	equivalent current through charging wire
Ja^{**}	modified Jakob number, $Ja^{**} = c_{p,f}\Delta T_{sub}/h_{fg}$
K	empirical coefficient
k	thermal conductivity
L	length
L_h	heated length of the charging cable
L_{th}	thermal entrance length
L_{uh}	unheated length of the charging cable
m	empirical constant used for the Badiuzzaman correlation
$\dot{m}$	mass flow rate through concentric annuli
n	empirical constant used in Shah's CHF correlation
M_W	molecular weight
Nu	Nusselt number
P	pressure
P_R	reduced pressure
Pr	Prandtl number
Q	heat transfer rate
Q_v	volumetric flow rate
q''	heat flux
q''_{CHF}	critical heat flux
R	parameter for uncertainty propagation
δR	uncertainty of the parameter
r	radius
r^*	radius ratio, $r^* = r_i/r_o$
R	electrical resistance
Re	Reynolds number
S	safety factor; suppression factor
T	temperature
t	time
tc	thermocouple

ΔT_{sat}	surface superheat, $\Delta T_{sat} = T_s$ - T_{sat}
ΔT_{sub}	fluid subcooling, $\Delta T_{sub} = T_{sat}$ - T_f
U	bulk fluid velocity
We_D	Weber number based on channel hydraulic diameter, $We_D = G^2 D_h/(\rho_f \sigma)$
We_L	Weber number based on heated length, $We_L = G^2 L_h/(\rho_f \sigma)$
X	variable for uncertainty propagation
δX	error of variable X
x_e	thermodynamic equilibrium quality
$x_{e,CHF}$	local thermodynamic equilibrium at CHF location
$x_{fd,t}$	fully developed thermal entrance length
Y	Shah's CHF correlating parameter
z	axial location

Greek symbols

α	temperature coefficient of charging wire
μ	dynamic viscosity
ν	specific volume; kinematic viscosity
ψ	dimensionless heat transfer rate
ψ_0	dimensionless heat transfer rate corresponding to $x_e = 0$
ρ	density; electrical resistivity of charging wire
σ	surface tension; standard deviation
θ	percentage predicted within ±30 %
ξ	percentage predicted within ±50 %

Subscripts

dv	developing
exp	experimental
f	liquid; bulk fluid
fd	fully developed
g	vapor
H	heated
i	inner tube of concentric annuli
in	test module inlet
max	maximum
nb	nucleate boiling
o	outer tube of concentric annuli
out	test module outlet
pred	predicted
s	surface
sat	saturation
sc	subcooled boiling
sp	single-phase
th	thermal
z	location along axial direction

Acronyms

AC	Alternating Current
AWG	American Wire Gauge
BEV	Battery Electric Vehicle
CHF	Critical Heat Flux
DAQ	Data Acquisition System
DC	Direct Current
DNB	Departure from Nucleate Boiling
FDB	Fully Developed Boiling
ICEV	Internal Combustion Engine Vehicle
LCC	Local Condition Correlation
MAE	Mean Absolute Error (%)
ONB	Onset of Nucleate Boiling
PDB	Partially Developed Boiling
RTD	Resistance Temperature Detector
TC	Thermocouple
UCC	Upstream Condition Correlation

1. Introduction

To mitigate the environmental issues associated with internal combustion engine vehicles (ICEVs), extensive research has been conducted on the development and performance optimization of eco-friendly energy technologies, such as fuel cells [1–8]. Electric vehicles (EVs) are gaining attention as a sustainable alternative capable of reducing greenhouse gas emissions and improving energy efficiency [9]. One of the major challenges hindering the widespread adoption of EVs is their longer charging time compared to ICEVs [10]. To address this issue, various approaches have been explored, leading to the development of direct current (DC) fast charging systems, which can significantly reduce charging time by increasing charging power. This increase in charging power also raises the

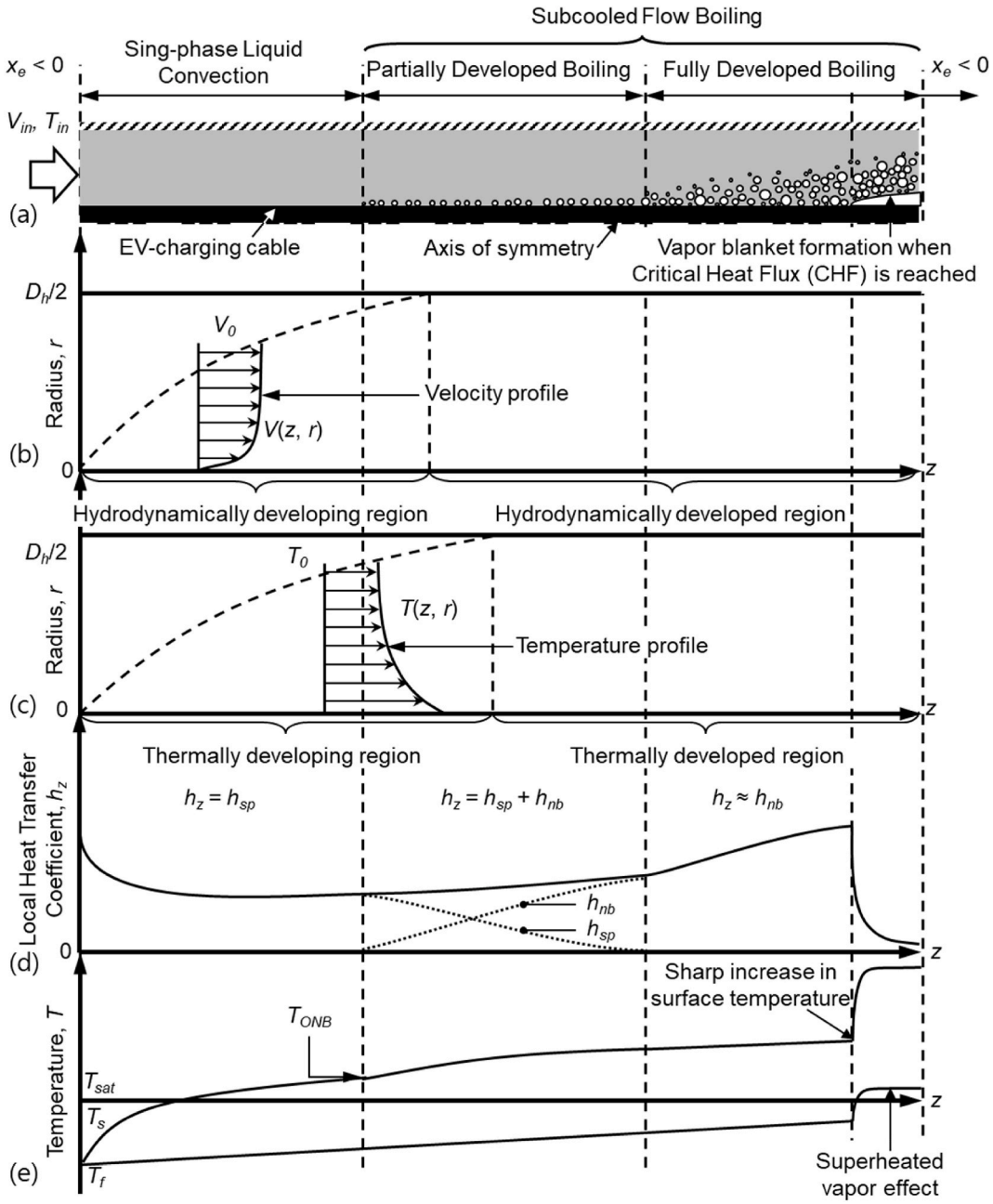

Fig. 1. Schematic representation of (a) the transport behavior of subcooled flow boiling with axial variations of (b) flow velocity profile in the radial direction, (c) temperature profile in the radial direction, (d) local heat transfer coefficient, and (e) fluid and surface temperature profiles in concentric annuli.

generation of Joule heat, creating a need for effective thermal management to prevent overheating and ensure user safety [11]. Recently, one of the authors of this work demonstrated the possibility of using subcooled flow boiling for the thermal management of charging cables [12]. However, further investigation is required to understand the complicated flow physics involved in subcooled flow boiling of dielectric fluids in concentric annuli to effectively implement this cooling technique in charging cable thermal management systems.

The test module for EV charging cable assemblies can be designed as concentric annuli with an inner heated surface, with the electric conductor positioned at the center of the cable assembly [12]. The axial flow regions transition from single-phase convection to partially developed boiling (PDB) and fully developed boiling (FDB) as convective heat transfer decreases and nucleate boiling increases within concentric annuli, as shown in Fig. 1(a). The single-phase convection transitions from a hydrodynamically and thermally developing region to a hydrodynamically developed but thermally developing region, and ultimately, to a hydrodynamically and thermally developed region, as illustrated in Fig. 1(b) and (c). The hydrodynamically developed region is shorter than the

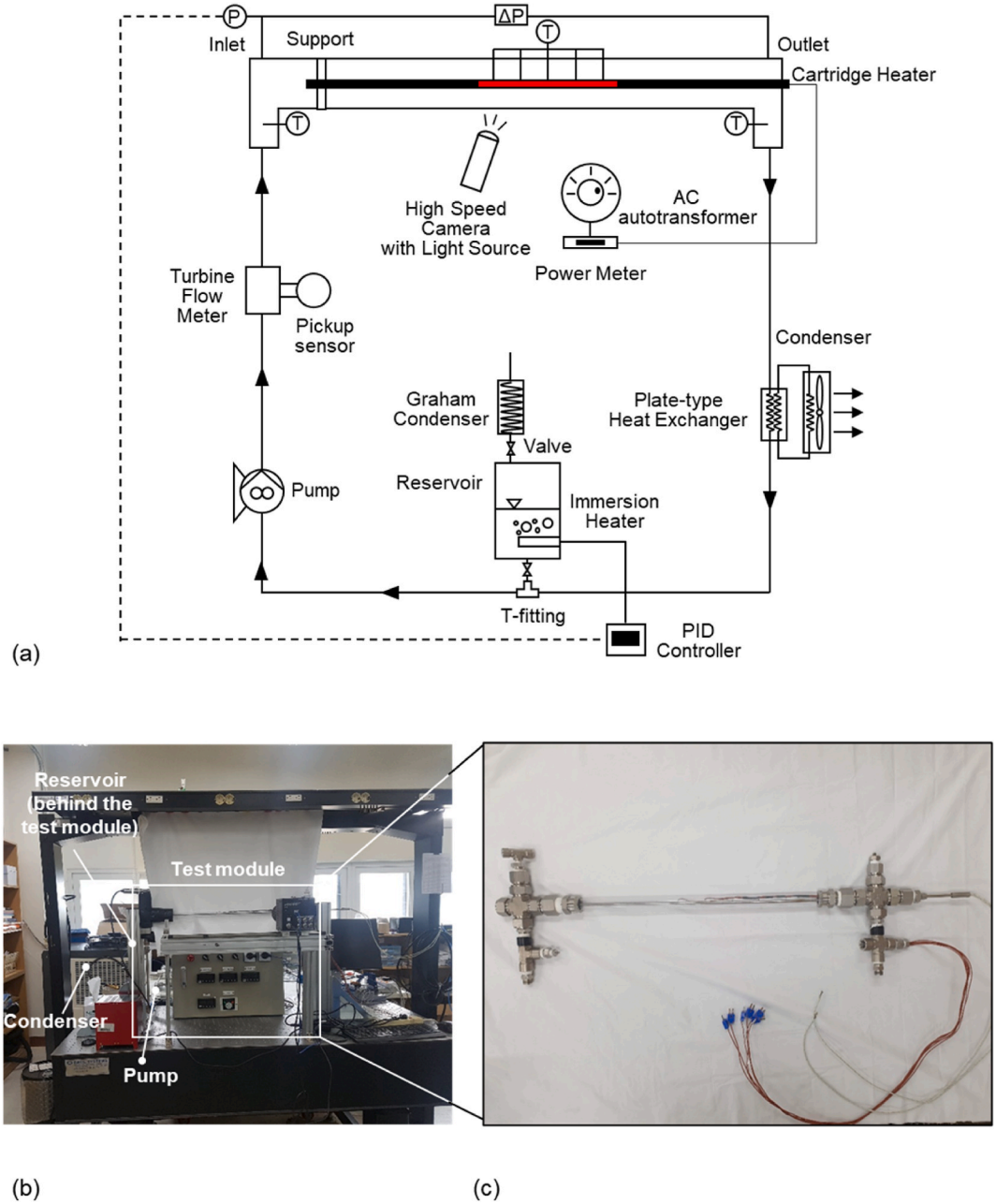

Fig. 2. A two-phase flow test loop consists of a test module, fluid reservoir, pump, plate-type heat exchanger, condenser, and other components. (a) A schematic diagram of the loop, (b) a photo of the loop, and (c) an enlarged view of the test module.

thermally developed region because momentum diffusivity is higher than thermal diffusivity in the working fluid, i.e., dielectric liquid HFE-7100. The thermally developing region at the inlet exhibits a significantly higher heat transfer rate compared with that in the developed region, attributable to the steep temperature gradient from the heated surface to the bulk fluid, but this region is shortened by vigorous fluid mixing by eddies in turbulent flow [13]. Nucleate boiling begins near the cable inlet under high Joule heat conditions, initiating PDB, with nucleate boiling increasing along the axial direction as shown in Fig. 1(d) [14]. The surface temperature is saturated due to increased overall heat transfer, while the fluid temperature continuously increases due to the thermal energy supply from the charging cable in the axial direction, as illustrated in Fig. 1(e). Increased bubble population and density on the heated cable surface led to the formation of a vapor film at the end of the annuli, a phenomenon known as the departure from nucleate boiling (DNB) [15]. This vapor film hinders heat transfer due to the low thermal conductivity of vapor. In this context, the applicability of empirical correlations [16–21] for EV charger thermal management needs to be assessed, as prior experimental studies have primarily focused on DNB-type CHF for subcooled flows in circular tubes [22] or rectangular channels [23–25].

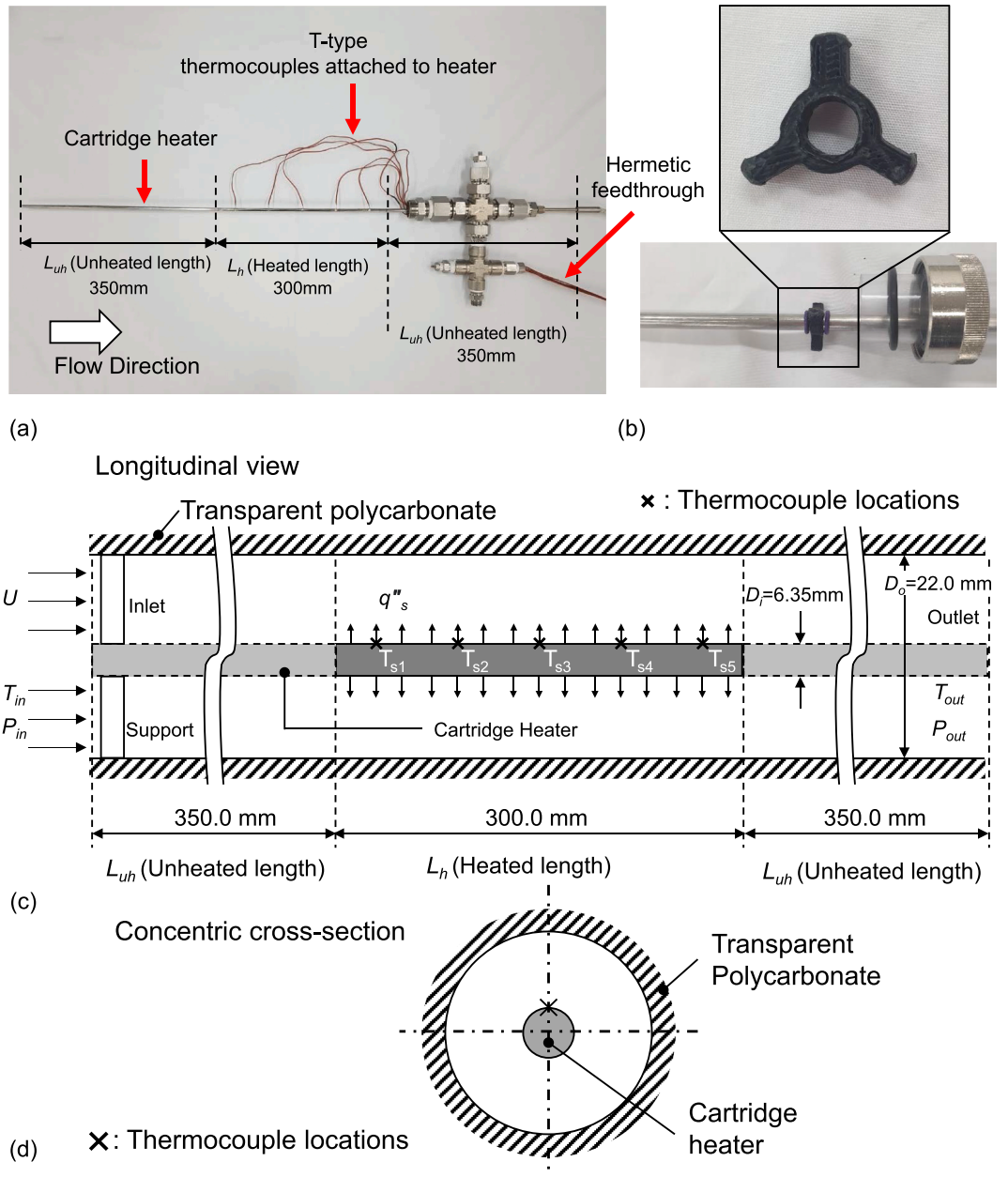

Fig. 3. The test module consists of a cartridge heater, thermocouples attached to the heater surface, and tube fittings. (a) A photo of the test module without the polycarbonate outer tube before assembly, (b) a 3D printed three-legged support for the heater installed inside the inlet fitting, schematic diagrams of (c) the module, and (d) the concentric cross-section.

Thus, this study is aimed at exploring the thermal characteristics of subcooled flow boiling in concentric annuli to assess the applicability of the proposed direct cooling technique for the thermal management of an ultra-fast EV charging cable. Specifically, this study investigates the possibility of leveraging subcooled flow boiling, which has the capability of suppressing surface temperature rise at high heat flux conditions, in practical cooling conditions, particularly in EV charging cables without an insulation layer. Experiments are conducted using a 30-cm test module, designed to simulate a 3–7 m long cable commonly used in commercial EV chargers. The test is conducted using a dielectric liquid, HFE-7100, flowing within concentric annuli featuring a heated inner surface and an adiabatic outer wall. Heat flux levels reaching up to 460,000 W/m^2 are tested, equivalent to a charging current of 3661 A, under various operating conditions, such as flow rates, inlet subcooling, and operating pressure, simulating ultra-fast charging scenarios. Flow characteristics under different operating conditions are investigated using high-speed flow images obtained through the transparent outer adiabatic tubes of the test module. In terms of flow characteristics, the thermal entrance effect, transition from PDB to FDB, and CHF trigger mechanism are examined. Furthermore, the accuracy of existing correlations used to predict the heat transfer coefficients and CHF are assessed to verify their validity for subcooled flow boiling in concentric annuli.

2. Experimental methods

2.1. Test loop

A two-phase flow test loop used to simulate the charging and cooling conditions of an EV charger is schematically shown in Fig. 2(a) with the corresponding facility photo provided in Fig. 2(b). As key components identified in Fig. 2(b), the test loop is primarily composed of four main components: a test module, a pump, a reservoir and a condenser. The test loop conditions the working fluid to the required inlet conditions for the test module, which is designed to handle the total amount of heat generation from the cable by Joule heating. This Joule heating is simulated by the cartridge heater, which is powered by an AC autotransformer and measured by the installed power meter. The changes in the flow pattern of subcooled flow boiling along the test module are captured by a high-speed camera, with the shutter speed ensured by a high-intensity light source. The 3M engineering dielectric fluid, HFE-7100, is selected as the working fluid and circulated by the gear pump installed upstream of the test module. The Micropump GLH series gear pump, which has the highest volumetric flow rate, $Q_{v,max}$, of 7.0 GPM, is magnetically coupled with a 0.75 kW LEESON AC motor. This gear pump was selected to minimize flow pulsations and ensure stable and consistent flow throughout the experiment. It regulates the flow rate by controlling the motor speed using an LS electric variable frequency drive. The volumetric flow rate, Q_v, is measured by the turbine flow meter, Omega FTB-1313, located downstream of the gear pump.

The heat acquired from the test module is released into the ambient atmosphere, where the air temperature is maintained constant by the laboratory air conditioner, causing the working fluid temperature to decrease to the desired test module inlet temperature. By adjusting the amount of heat exchange between the working fluid and the modular air cooler connected by the plate-type heat exchanger, the working fluid can be precisely tuned to the desired subcooled inlet condition. The constant pressure point installed in the downstream region controls the system and test module inlet pressures. The liquid reservoir is equipped with a 3 kW immersion heater and a PID controller to regulate the test module's inlet pressure by adjusting the amount of vapor it stores and is connected to the main flow loop through a T-type fitting. The non-condensable gas is removed before the working fluid is charged into the main loop by a Graham condenser, installed at the top of the reservoir. This condenser returns the heavier condensed liquid to the reservoir and discharges the lighter non-condensable gas into the atmosphere. The Graham condenser exchanges heat with a connected constant-temperature water bath. The entire loop's components are connected by half-inch stainless steel tubes, secured by Swagelok plastic clamp tube support kits at various locations to prevent the effects of vibration. All data readings are collected by the data acquisition system, National Instruments (NI) Compact DAQ, and displayed in the control box, enabling prompt responses to any abnormal operation or unexpected emergencies.

2.2. Concentric annuli test module

A partial assembly of the test module is presented in Fig. 3(a). The test module simulates the EV charging condition using a custom-made cartridge heater with a surface made of stainless steel 316 and a diameter of $D_i = 6.35$ mm, approximating the Joule heating from the wire of AWG3 with a diameter of 5.827 mm. The reason for using a slightly larger diameter cartridge heater compared to the AWG3 specification was to utilize commercially available standardized 1/4-inch (6.35 mm) fittings, which closely match the diameter of the AWG3 wire. The experimental results are presented in terms of heat flux to minimize differences in heat release rate, bubble generation, and two-phase flow characteristics that could arise from the size discrepancy. The surface heat flux is adjusted using an AC transformer (5.0 kVA, 0–240V) connected to the electrical lead wires of the heater. Five equidistantly spaced T-type thermocouples are silver-soldered along the heater using BAg-1, a 45 % silver brazing alloy known for its high thermal conductivity of 291 W/m-K, similar to that of copper wire having 385 W/m-K. This similarity contributes to accurate wire temperature measurement. In the process of soldering, special care is taken to use the minimum amount of solder alloy to avoid creating any additional junctions other than the thermocouple bead. The AWG24 thermocouple wires are sealed off and electrically connected to the DAQ using the hermetic feed-through fittings provided by RHSeals. A working fluid, HFE-7100, enters through the inlet T-shaped fitting (not shown in Fig. 3(a)), and flows over the wire conducting cooling. A pair of T-shaped fittings at the inlet and outlet is utilized to measure the pressure and the temperature using absolute pressure transducers and thermocouples. A pair of absolute and differential pressure transducers, OMEGA PX409-100A5V (100 psi) and PX409-015DWU5V (15 psi), installed at the inlet and outlet, were used to measure the pressure drop through the test module. As shown in Fig. 3(b), the 3D printed three-legged heater support installed at the inlet unsupported end holds the heater at the center to avoid any eccentricity of the concentric annuli that causes asymmetric heat transfer characteristics [26–28].

A longitudinal sectional view of the test module is shown in Fig. 3(c) and (d), where the heater is in the center of the concentric

annuli, which consists of cartridge heater and transparent polycarbonate tube that allows optical access to the flow patterns. The vacuum fittings (Swagelok Torr O-ring) were used at both ends of the polycarbonate tube to seal the flow path. The inner diameter of the polycarbonate tube is $D_o = 22.0$ mm which results in the hydraulic diameter of the concentric annuli $D_h = 15.65$ mm,

$$D_h = \frac{4A_{ch}}{P_F} = D_o - D_i. \tag{1}$$

The heated section spans 300.0 mm in the middle of the heater, with unheated sections of 350.00 mm in upstream and downstream regions, respectively. The 300.0 mm heated section was specifically selected as it represents the maximum length for which a high heat flux cartridge heater, capable of simulating the Joule heating conditions expected in ultra-fast EV charging cables, could be manufactured. This length was also sufficient to allow for the clear observation and analysis of critical aspects such as the transition of flow regimes and heat transfer mechanisms, and the occurrence of CHF due to vapor accumulation. These observations are essential for accurately predicting the thermal performance of actual EV charging cables. The locations of thermocouples, equidistantly placed along the heated section, along with other geometry information, are provided in Table 1. A 13 mm thick synthetic rubber foam (HiFlex) was applied over the entire test loop for insulation purposes, except for the test module's flow visualization region. The cross-sectional structure of the concentric annuli used in this study is shown in Fig. 3(d), clearly illustrating the concentric arrangement between the cartridge heater and polycarbonate applied in the experiment.

2.3. Instrumentation and measurement accuracy

The flow visualization is conducted using a Photron Fastcam Mini AX100 high-speed camera equipped with a Nikkor 105 mm micro-lens, with lighting provided by a Revox SLG-150V high-intensity LED optical source. The UV filter is used to capture clear images with a sharp interface between liquid and vapor in a two-phase flow. Even though the maximum shutter speed of the camera is 1/540,000 s, it is adjusted to 1/8500 s to ensure reasonably high image resolution and field of view under the given quantity of light from the LED optical source.

The fluid temperatures at the test module inlet and outlet are measured by sheathed, ungrounded T-type thermocouples. All thermocouples, including those used for the test module, are calibrated simultaneously over the temperature range of −15 to 95 °C. This calibration is conducted using the AND company model AD-RC08 thermal water bath and an Omega platinum Pt 100 PR-10-2-100-1/8-6-E 1/8-inch diameter resistance temperature detector (RTD) sensor. A 50-50 % volume mixture of ethylene glycol and water is used as a bath fluid to prevent freezing in the temperature range below zero. All thermocouples and RTD are tied together and positioned in one spot within the thermal bath to ensure temperature uniformity, and the temperature is measured at intervals of 2.5 °C. The resistance outputs from the RTD are converted into temperature using the European standard curve (ITS-90) with a temperature coefficient of resistance $\alpha = 0.00385\ \Omega/\Omega/°C$. All temperature measurements from thermocouples are correlated against the RTD outputs using a least squares regression to yield third-order polynomials. The measurement accuracy of T-type thermocouples is 1.0 °C, while that of RTDs is 0.15 °C, respectively. On the other hand, the calibrated thermocouples demonstrated the enhanced accuracy, with error measured less than 0.5 °C.

Yokogawa WT310E power meter is installed between the heater and AC autotransformer to measure the voltage, current, and power input to the heater. All data signals collected by the process meters in the control box are transmitted to the NI-9214 and 9205 data acquisition (DAQ) system. The measured readings are monitored and stored on the computer using LabVIEW software. To prevent any noise in the measured data, the DAQ system is grounded to the optical table. The measurement errors and uncertainties for various parameters are presented in Table 2. The uncertainty propagated in calculation of the heat transfer coefficient, pressure drop, and vapor quality increment were estimated using the root sum square method [29,30] based on sensor errors as,

$$\delta R = \sqrt{\left(\frac{\partial R}{\partial X_1}\delta X_1\right)^2 + \left(\frac{\partial R}{\partial X_2}\delta X_2\right)^2 + \cdots}\ . \tag{2}$$

where δX is a known error of variable X, and δR is an uncertainty of the parameter R.

2.4. Experimental procedures

Prior to charging the system, the liquid reservoir and test loop are separated by closing the valve installed between the two parts. The test loop is kept evacuated while the liquid reservoir is filled with the liquid-state working fluid, HFE-7100 ($T_{sat} = 61$ °C at P = 101 kPa). The non-condensable gases in the working fluid are removed through the degassing process. The non-condensable gases are separated from the liquid-state working fluid through vigorous boiling conducted by the immersion heater. The vapor and non-condensable mixture are then directed to pass through the Graham condenser by opening the valve situated on top of the reservoir. Utilizing the saturation temperature difference, the Graham condenser, equipped with a cooling channel, condenses the vapor back into liquid and purges the non-condensable gases into the atmosphere. After repeating the degassing process several times to ensure the

Table 1
Dimensions of the concentric annuli test module.

Heated length, L_h [mm]	Outer diameter, D_o [mm]	Inner diameter, D_i [mm]	Hydraulic diameter, D_h [mm]	Axial locations of thermocouples measured within the heated length [mm]
300	22	6.35	15.65	25, 87.5, 150, 212.5, 275

Table 2
Measurement error and uncertainty propagation.

Variable	Sensor models	Error	Reason	Parameter	Uncertainty	Reason
Absolute pressure	PX409-100A5V, OMEGA	±0.08 %	Model errors*	Heat transfer coefficient, h	≤5 %	Errors from power meters, thermocouples, and size of cartridge heater
Differential pressure	PX409-015DWUV, OMEGA	±0.08 %	Model errors*	Pressure drop, ΔP	≤0.1 %	Pressure sensor errors
Surface thermocouple temperature	24AWG (T-type), RHSeals	±1.0 °C	Model errors*	Thermodynamic equilibrium quality change, Δx_e	≤1.75 %	Errors from pressure sensor and thermocouples.
RTD temperature	PR-10, OMEGA	±0.15 °C	Model errors*			
Mass flow rate, $\dot{m}$	FTB-1313, OMEGA	±0.1 %	Model errors*			
Heat input, Q	WT310E, YOKOGAWA	±0.1 %	Model errors*			
Length of the cartridge heater	Custom-made	+1 %	Manufacturing errors**			
Radius of the cartridge heater	Custom-made	+1.6 %	Manufacturing errors**			

Model errors*: The error level of the sensor as specified by the product manufacturer.
Manufacturing errors**: The discrepancies that occurred during the actual production process compared to the custom specifications requested.

removal of non-condensable gases, the separating valve is opened to charge the test loop. Once the system is charged, the system pressure is maintained higher than the atmospheric pressure by boiling a liquid in reservoir to prevent the infiltration of non-condensable gases.

As a first step, the inlet pressure of the test module is controlled by the amount of vapor stored in the liquid reservoir. A PID controller maintains the set pressure by adjusting the amount of heat input to the immersion heater based on the signal from the inlet pressure. The mass flow rate is set by the variable frequency drive, which adjusts the speed of the AC motor in the pump assembly. The testing heat flux is set after confirming the adiabatic flow condition by ensuring that the power input to the heater is zero when the brush of the AC autotransformer is set to zero. The heat flux is tested up to the maximum heater capacity or until the critical heat flux (CHF) occurs. By carefully monitoring the system, the test module is protected from the critical heat flux (CHF), which can be identified by vapor blanket formation, by immediately powering off the heater. The inlet temperature of the test module is manually regulated by the subcooled condenser, utilizing data from the inlet thermocouple measurements. The data are recorded once the system has operated for 30 min or when the steady-state condition is attained.

2.5. Data reduction

The heat flux and mass velocity play a critical role in determining the thermal management effectiveness of EV charging systems. Table 3 offers a detailed explanation of these key parameters, including their physical meaning, impact on cooling, and related dimensionless numbers. This information aims to enhance readers' understanding of the subsequent calculations and the relevance of each parameter to the cooling performance observed in the experiments.

The flow in this study possesses a concentric annular cross-section and is assumed to exhibit an adiabatic outer boundary condition. In the experiment, the surface heat flux on the heated length surface of the heater can be calculated by

$$q_s'' = \frac{Q}{A_H}, \tag{3}$$

where the amount of heat generation, Q, is measured by the power input to the heater and the heated surface area, A_H, which is calculated by

$$A_H = \pi D_i L_H \ . \tag{4}$$

D_i and L_H are the heater diameter and heated length. To estimate the surface heat flux on the wire during EV charging, Joule heating is calculated by

Table 3
Explanation of key parameters and their impact on cooling performance in EV charging systems.

Parameters	Physical meaning in EV charger system	Impact on cooling	Related dimensionless numbers
Heat flux, q_s''	The Joule heating of the cable, directly proportional to the charging current	Higher heat flux increases cooling demand and lead to higher surface temperatures and potential CHF occurrence.	Nusselt number (Nu), Boiling number (Bo)
Mass velocity, G	The mass of coolant flowing per unit cross-sectional area of the system's internal loop.	Increased mass velocity enhances convective heat transfer, delays ONB, and CHF	Reynolds number (Re), Prandtl number (Pr)

$$Q = RI_{wire}^2, \tag{5}$$

where R and I_{wire} are the resistance and current of the wire, respectively. The electrical resistance of a wire is calculated by using Pouillet's law,

$$R = \frac{\rho L_h}{A_{ch,i}}, \tag{6}$$

where $A_{ch,i}$ is the cross-sectional area of the charging cable. The change in the resistivity of copper wire, ρ, with respect to temperature increase from the reference temperature, $T_{20^\circ C}$, is expressed by

$$\rho = S\rho_{20^\circ C}(1 + \alpha\Delta T) = S\rho_{20^\circ C}(1 + \alpha(T - T_{20^\circ C})) \text{ for } T \geq 20^\circ C, \tag{7}$$

where the temperature coefficient of $\alpha = 4.29 \text{ x } 10^{-3}$ K^{-1} and safety factor of $S = 1$ are assigned. For temperatures below 20 °C, the resistivity of copper is estimated by

$$\rho = \rho_{20^\circ C} \text{ for } T < 20^\circ C, \tag{8}$$

where $\rho_{20^\circ C} = 1.724 \text{ x } 10^{-8}$ Ωm. The conversion chart between heat flux, power input, and EV charging current is presented in Table 4. The thermophysical properties of HFE-7100 are provided by the supplier, 3M company, and are used to estimate the flow parameters. The mass velocity, G, is calculated by

$$G = \frac{Q_v}{v_f|_{T_{in}} A_{ch}}, \tag{9}$$

where Q_v is the volume flow rate, which represents the time-averaged value after the system reached a steady state. This flow rate is regulated by a high-precision gear pump that was selected to minimize flow pulsations, and $v_f|_{T_{in}}$ is the specific volume of saturated liquid at the test module inlet temperature, T_{in}. The cross-sectional area of a concentric annuli, A_{ch}, is calculated by

$$A_{ch} = \frac{\pi}{4}\left(D_o^2 - D_i^2\right). \tag{10}$$

Table 5 provides the conversion chart between Q_v, V, and G at a temperature of 20 °C. The thermodynamic equilibrium quality, x_e, is calculated by

$$x_e = \frac{h - h_f|_p}{h_{fg}|_p}, \tag{11}$$

where $h_f|_p$ and $h_{fg}|_p$ are the enthalpies of saturated liquid and evaporation at a given pressure, respectively.

The fluid enthalpies, h, are assessed at the inlet and outlet for $x_{e,in}$ and $x_{e,out}$, and h_{in} and h_{out} are calculated by

$$h_{in} = h_f|_{T_{in}} + v_f|_{T_{in}}\left(P_{in} - P_{sat}|_{T_{in}}\right), \tag{12}$$

and

$$h_{out} = h_{in} + Q/\dot{m}. \tag{13}$$

$P_{sat}|_{T_{in}}$ is the saturation pressure corresponding to the inlet temperature. In Eq. (13), h_{out} is estimated by applying the energy conservation law to the test module using the measured mass flow rate. The amount of subcooling is calculated by

$$\Delta T_{sub} = T_{sat}|_P - T_f, \tag{14}$$

where $T_{sat}|_P$ and T_f represent the saturation temperature and fluid temperature at the inlet and outlet, respectively.

The local heat transfer coefficient at any axial location 'z' can be calculated by

Table 4
Conversion chart of power input to equivalent EV charging current I_{wire}.

Power input, Q	Heat flux, q_s''	EV charging current, I_{wire}
[W]	[W/m^2]	[A]
598	100,000	1707
1197	200,000	2414
1795	300,000	2957
2394	400,000	3414
2753	460,000	3661

Table 5
Conversion chart of volume flow rate to mass flux G.

Volume flow rate, Q_v [m^3/s]	Mean velocity, V [m/s]	Mass flux, G [kg/m^2s]
$4.21X10^{-5}$	0.12	183.47
$7.71X10^{-5}$	0.22	336.36
$1.12X10^{-4}$	0.32	489.24
$1.47X10^{-4}$	0.42	642.13
$1.82X10^{-4}$	0.52	795.02
$2.17X10^{-4}$	0.62	947.91
$2.52X10^{-4}$	0.72	1100.80
$2.87X10^{-4}$	0.82	1253.69

$$h_z = \frac{q_s''}{T_{s,z} - T_{f,z}}, \tag{15}$$

where $T_{s,z}$ is the measured local heater surface temperature and $T_{f,z}$ a local fluid temperature. $T_{f,z}$ is calculated by axial interpolation between $T_{f,in}$ and $T_{f,out}$ applying the energy balance and considering sensible heat transfer only. The axial conduction through the heater is neglected, and q_s'' is assumed to be axially uniform. The key parameters in the present study are summarized in Table 6.

3. Results and discussion

3.1. Validation of wire surface temperature measurement technique with single-phase flow

The accuracy of surface temperature measurements was indirectly validated by comparing experimental and predicted surface temperatures in single-phase flow under various operating conditions, as illustrated in Fig. 4: (a) heat flux, (b) mass velocity, and (c) inlet fluid temperature. With high agreement demonstrated in all single-phase test cases, the accuracy of temperature measurements in subcooled flow boiling experiments was reliably ensured. Depending on the growth of the thermal boundary layer and the axial variations of the heat transfer coefficient, the surface temperature exponentially saturates in the thermally developing region and linearly increases according to the axial increase of fluid temperature in thermally developed region. The heat transfer coefficient rapidly decreases along the tube in the thermally developing region, and then it remains almost constant in the thermally developed region. The growth of the thermal boundary layer and heat transfer coefficient primarily vary with mass velocity. A decrease in surface temperature and an increase in thermal entrance length were observed with an increase in mass velocity, as shown in Fig. 4(b). With almost the same axial heat transfer coefficient trends, the surface temperature increases with heat flux and inlet temperature, as shown in Fig. 4(a) and (c).

For the flows in the concentric annuli, the Reynolds number [31],

$$\mathrm{Re}_l = GD_l \Big/ \mu_f, \tag{16}$$

is defined by using a laminar equivalent diameter [32],

$$D_l = D_h \frac{1 + r^{*2} + (1 - r^{*2})/\ln r^*}{(1 - r^*)^2}, \tag{17}$$

where r^* is the ratio of the inner to outer tubes' radii, $r^* = r_i/r_o$ [32]. All experimental test cases in present study involve only turbulent flows, with Reynolds numbers defined in Eq. (16) ranging from 2534 to 19,430, which are higher than the critical Reynolds number, Re_{crit}, of 2450 where laminar-turbulent transition occurs [31]. As HFE-7100 used in the present study has a Pr number higher than 9, the thermal entrance length is assumed to be $L_{th} \cong 5D_l$ for fully developed inlet velocity profile [13]. This value is determined by the definition of thermal entrance length, which is based on the local heat transfer coefficient required to reach within 5 % of the fully developed value with $\mathrm{Pr} = 10$. With the theoretically determined hydrodynamic entrance length, L_{hy} [33], the thermal entrance length, L_{th}, is determined by [34]

Table 6
Summary of operating conditions.

Parameters	Values
Mass velocity, G	183.47–1253.69 kg/m^2s
Volume flow rate, Q_v	4.21 x 10^{-5} – 28.74 x 10^{-5} m^3/s
Test module inlet pressure, P_{in}	118.45–212.34 kPa (17.18–30.80 psia)
Test module outlet pressure, P_{out}	101.00–207.95 kPa (17.03–30.16 psia)
Charging cable surface heat flux, q_s''	20,000–460,000 W/m^2
Equivalent current through charging wire, I_{wire}	763–3661 A

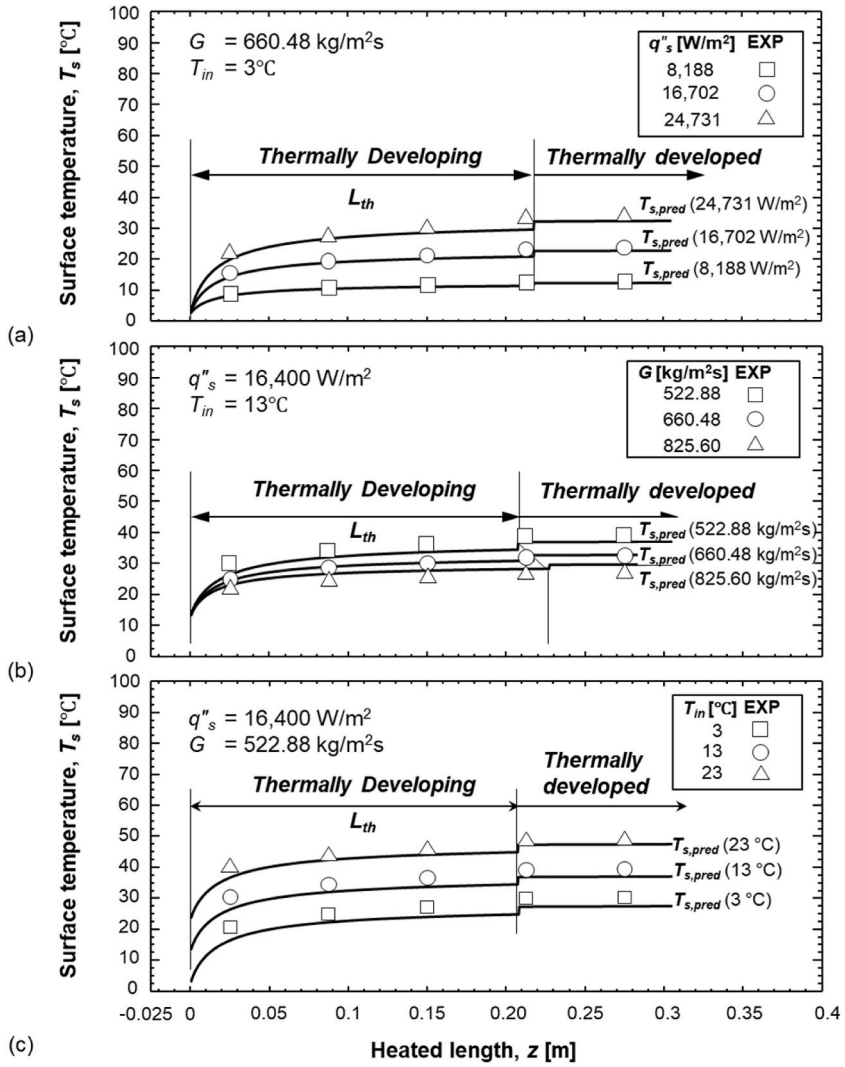

Fig. 4. Validation of the measured axial temperatures on the inner heating surface for the single-phase flow in concentric annuli with the solution obtained by Kays and Leung. Each plot represents the effects of (a) heat flux, (b) mass velocity, and (c) inlet fluid temperature.

$$L_{th} \cong 1.3590 \mathrm{Re}_l^{1/4} D_l + 5 D_l. \tag{18}$$

Due to the lack of validated empirical correlations, Al-Arabi's relation for the Nusselt number in thermally developing flows in circular tubes [35],

$$Nu_{dv,th} = Nu_{fd,th}\left[1 + \frac{\left(0.68 + \frac{3000}{\mathrm{Re}_f^{0.81}}\right)}{\left(L_{sp}/D_h\right)^{0.9} \mathrm{Pr}_f^{1/6}}\right], \tag{19}$$

is adopted for concentric annuli by combining it with the fully developed Nusselt number, $Nu_{fd,th}$,which is calculated using Kays and Leung's table for turbulent flows in concentric annuli [36]. As shown in Fig. 5, a small MAE of 8.63 % for 40 data points in the comparison between experimental and predicted heat transfer coefficients validates the accuracy of surface temperature measurement. MAEs were confirmed to be 15.42 %, 6.66 %, 7.38 %, 7.78 %, and 5.73 % at heated length locations $z = 25.0$, 87.5, 150.0, 212.5, and 275 mm, respectively, and errors were estimated to be relatively larger at the near inlet location ($z = 25.0$ mm) due to strong thermal entrance effects.

3.2. Demarcation between PDB and FDB in subcooled flow boiling regimes

As the heat transfer mechanism changes depending on the subcooled flow boiling regimes, it is necessary to demarcate between

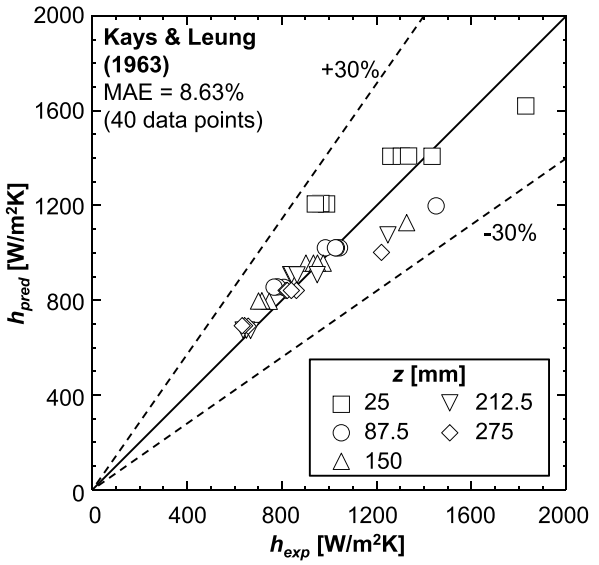

Fig. 5. Validation of experimental data with the predicted solution by Kays and Leung's relation for the heat transfer coefficient of single-phase flow in concentric annuli.

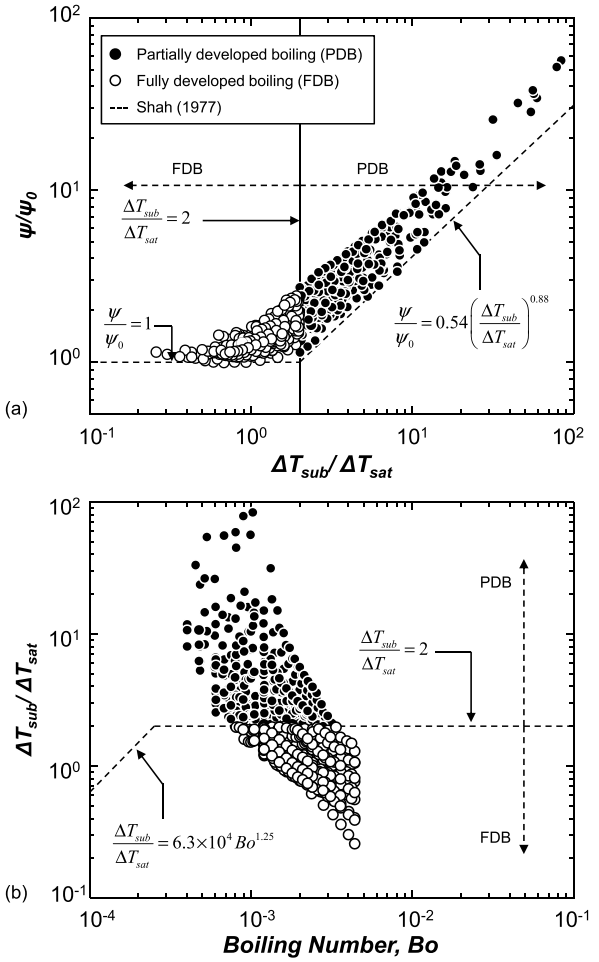

Fig. 6. Demarcation of experimental subcooled flow boiling data points into the partially developed boiling (PDB) and fully developed boiling (FDB) regimes using Shah's relation. (a) Ratio of dimensionless heat transfer rate, ψ/ψ_0, versus $\Delta T_{sub}/\Delta T_{sat}$, and (b) $\Delta T_{sub}/\Delta T_{sat}$ versus boiling number, *Bo*.

PDB and FDB to enhance the understanding of the transport phenomena and heat transfer mechanisms in concentric annuli. In designing a practical two-phase cooling system for an EV charger, it is essential to provide information about the axial location of flow regime transition and the extent to which specific heat transfer mechanisms dominate. The single-phase subcooled liquid flow enters the test module and absorbs sensible heat along the channel. Both the fluid and surface temperatures increase in the axial direction. When the surface temperature reaches the ONB temperature [37],

$$T_{s,ONB} = T_{sat} + \frac{4\sigma T_{sat} h_{sp,f}}{k_f h_{fg} \rho_g} \left(1 + \sqrt{1 + \frac{k_f h_{fg} \rho_g}{2\sigma T_{sat} h_{sp,f}} \left(T_{sat} - T_f \right)} \right), \tag{20}$$

the first bubble is generated, indicating the initiation of the subcooled flow boiling regime. The 'h' in Eq. (20) indicates the single-phase heat transfer coefficient, which is estimated by [38,39].

$$h_{sp,f} = 0.023 \mathrm{Re}_{fo}^{0.8} \, \mathrm{Pr}^{0.4} \frac{k_f}{D_h}. \tag{21}$$

In the following PDB region, more bubbles appear along the channel as more cavities are activated by increased surface superheat, ΔT_{sat}. The cavities are activated when the 'available' superheat exceeds the 'required' superheat, which is determined by the size of the cavity and the fluid properties. The growth of bubbles in the PDB region is strongly suppressed by the re-condensation effect from the highly subcooled bulk flow. Balancing the amount of evaporation and condensation, these bubbles attach to the surface and slide along the channel while maintaining their size. Despite of enhanced by these bubble motions and latent heat for evaporation, the dominant heat transfer mechanism in PDB is still single-phase convection due to the low population of bubbles. In the FDB region, the dominant heat transfer mechanism transitions to nucleate boiling due to an increase in activated nucleation sites and reduced single-phase convection caused by the limited contact of bulk liquid with the heated surface. By reducing the non-thermal equilibrium state through an increased amount of re-condensation into subcooled bulk liquid, followed by an increase in bulk fluid temperature, the enhanced bubble generation and growth expedite the transition of the heat transfer mechanism to nucleate boiling in the FDB regime.

763 experimental data, 314 PDB and 449 FDB, are examined and sorted into PDB and FDB regimes based on Shah's two criteria for demarcation as shown in Fig. 6 [40]. In the first criterion, Shah suggested the dimensionless subcooling, $\Delta T_{sub}/\Delta T_{sat}$, of 2 as the transition borderline from PDB to FDB. Subcooled flow boiling regimes are demarcated by the ratio of surface superheat and fluid subcooling as follows,

$$\frac{q_s'' / \left(h_{sp} \Delta T_{sat} \right)}{\psi_0} = \frac{\psi}{\psi_0} = \begin{cases} 0.54 \left(\dfrac{\Delta T_{sub}}{\Delta T_{sat}} \right)^{0.88}, \dfrac{\Delta T_{sub}}{\Delta T_{sat}} > 2 \\ 1, \dfrac{\Delta T_{sub}}{\Delta T_{sat}} \le 2 \end{cases}. \tag{22}$$

ψ is the dimensionless heat transfer rate expressed by

$$\psi = \frac{q_s''}{h_{sp,f} \Delta T_{sat}}, \tag{23}$$

and ψ_0 is ψ when the thermodynamic quality is zero, $x_e = 0$, having the following relation with the boiling number, $Bo = q_s'' / G h_{fg}$, as

$$\psi_0 = \begin{cases} 230 Bo^{0.5}, Bo > 0.3 \times 10^{-4} \\ 1 + 46 Bo^{0.5}, Bo < 0.3 \times 10^{-4} \end{cases}. \tag{24}$$

The proportion of single-phase convection in the PDB region increases as the flow is further subcooled, while the contribution of single-phase convection saturates approaching $\psi/\psi_0 = 1$ in the FBD region. The overall trend of the experimental data in this study deviates from Shah's prediction due to the unpredictable activation of cavities on the heated surface. This activation is influenced by the sequence of increasing and decreasing heat flux or subcooling, which varies across different studies [40]. Shah further demarcated the transition using $\Delta T_{sub}/\Delta T_{sat}$ and Bo by

$$\text{PDB (high subcooling)} : \frac{\Delta T_{sub}}{\Delta T_{sat}} > 2 \text{ or } \frac{\Delta T_{sub}}{\Delta T_{sat}} > 6.3 \times 10^4 Bo^{1.25}, \tag{25}$$

and

$$\text{FDB (low subcooling)} : \frac{\Delta T_{sub}}{\Delta T_{sat}} \le 2 \text{ and } \frac{\Delta T_{sub}}{\Delta T_{sat}} \le 6.3 \times 10^4 Bo^{1.25}. \tag{26}$$

As the proportion of single-phase convection to total heat transfer decreases when nucleate boiling becomes dominant, an inversely proportional relationship between $\Delta T_{sub}/\Delta T_{sat}$ and Bo is observed, as shown in Fig. 6(b). This relationship arises because the intensity of nucleate boiling, represented by Bo, is directly proportional to the rate of thermal energy supply for the heated surface, indicated by available surface superheat ΔT_{sat}, and inversely proportional to the rate of condensation by the bulk fluid, represented by local subcooling ΔT_{sub}.

3.3. Boiling curves and axial variations of heat transfer mechanisms: Effects of strong thermal non-equilibrium flows undergoing flow regime transitions in the thermally developing region

Boiling curves are essential tools for analyzing heat transfer performance in two-phase flow systems. These curves typically illustrate the relationship between surface superheat (x-axis) and surface heat flux (y-axis), where surface superheat is defined as the difference between the surface temperature and the saturation temperature. Boiling curves help in understanding how heat is transferred across various heat transfer regimes, such as single-phase convection and nucleate boiling. This understanding is particularly valuable for optimizing thermal management strategies in applications like electric vehicle (EV) charging cables. Fig. 7(a) presents the local boiling curves at five axial positions of the heated module for a mass velocity of $G = 476.61$ kg/m^{2}s. At the lowest heat flux, $q_s'' = 20{,}000$ W/m^2, all positions fall within the single-phase convection cooling regime, where the bulk fluid temperature and surface temperature both rise linearly with the heat flux. As the heat flux reaches $q_s'' = 60{,}000$ W/m^2 at the upstream position ($z = 0.0250$ m), a reduction in surface superheat is observed, indicating the onset of nucleate boiling (ONB) on the heated surface. As heat flux increases, the boiling curve slope at all positions follows a power-law trend, indicating that nucleate boiling suppresses surface temperature rise. At the downstream position ($z = 0.2750$ m), where subcooling decreases, nucleate boiling dominates, resulting in a steeper slope. This suggests that subcooled flow boiling offers advantages for thermal management in cables. Fig. 7(b) shows the average surface superheat versus mass velocity (G) at five axial positions. Due to the enhanced convective heat transfer at higher mass velocity ($G = 1100.80$ kg/m^{2}s), a higher heat flux is required to reach ONB compared to the lower mass velocity ($G = 183.47$ kg/m^{2}s). ONB occurs across several heat flux ranges because the upstream remains in single-phase convection, while the downstream reaches ONB due to the reduced bulk fluid subcooling. Even at high heat flux, increasing mass velocity effectively reduces surface superheat, indicating that entrance effects in the short experimental module can improve overall cooling performance. Although this study did not conduct a comprehensive experiment on the degree of inlet subcooling, it is important to note that subcooling significantly impacts the heat transfer performance in subcooled flow boiling. Higher subcooling delays the ONB, prolonging the single-phase flow where the heat transfer coefficient is not significantly affected by the degree of subcooling. When boiling does initiate, increased subcooling can suppress nucleate boiling, which may result in a lower heat transfer coefficient under the FDB regime, while also delaying the formation of a vapor blanket or dryout, effectively raising the CHF.

In the subcooled flow boiling regime, analyzing the axial heat transfer mechanisms of the experimental module allows for the prediction of the thermal performance of actual charging cables, providing useful design guidelines for improving cooling efficiency. This analysis is crucial as the coupling effect between the suppression of single-phase convection in the thermally developing region

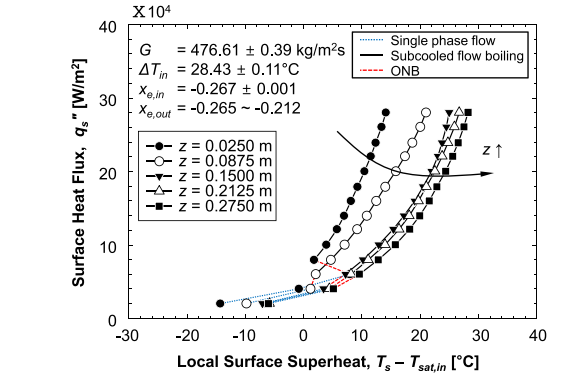

Fig. 7. (a) Local boiling curves for $G = 476.61$kg/m^{2}s at different axial locations. (b) Boiling curves with average surface superheat for different mass velocities.

and the enhancement of two-phase nucleate boiling downstream of the ONB location influences the axial variation of the local heat transfer coefficient. This mechanism can maintain surface temperatures more stably as nucleate boiling heat transfer increases downstream, making it particularly useful for thermal management in electric vehicle charging cables.

Subcooled boiling in horizontal annuli exhibits unique characteristics. The curvature of the inner surface of the annular structure promotes bubble detachment from the heated surface, and buoyancy causes bubbles to migrate upward, leading to circumferentially uneven heat transfer. Circular tubes, with their symmetrical shape, tend to have a more uniform bubble distribution, whereas in rectangular channels, bubbles may accumulate in the corners. These differences in bubble dynamics due to the shape of the tubes significantly impact overall heat transfer performance. The interaction between the fluid's surface tension and the tube shape also influences bubble nucleation density and departure frequency, which in turn affects heat transfer efficiency [41,42]. With the development of the thermal boundary layer, the convective heat transfer coefficient rapidly decreases along the axial direction until it

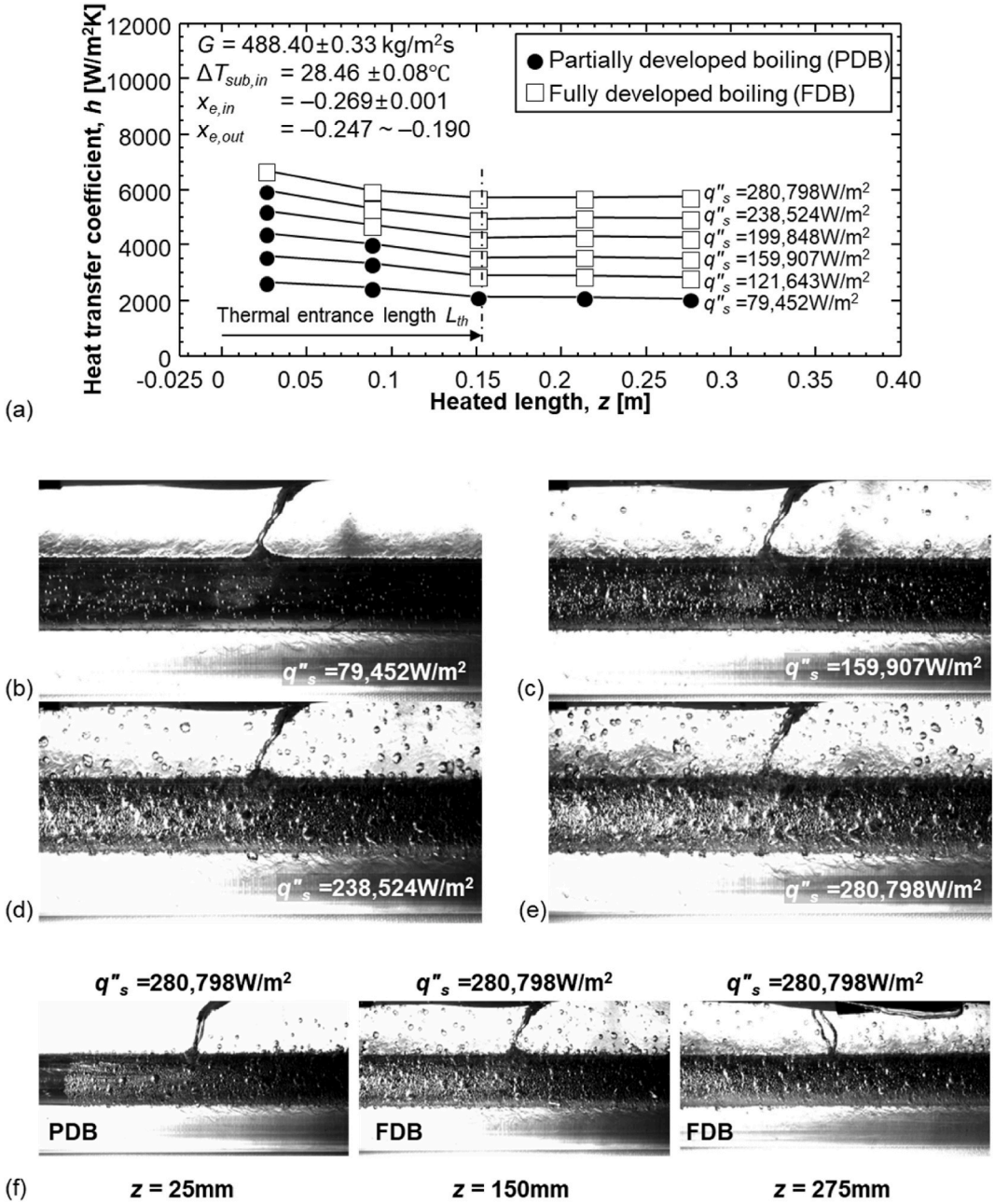

Fig. 8. (a) Axial variations of the experimental heat transfer coefficient on the inner heating surface for subcooled flow boiling in concentric annuli with varying heat flux q''_s according to the change of the heated length z. Flow visualization images at $z = 150$ mm with heat fluxes of (b) $q''_s = 79{,}452$ W/m^2, (c) $q''_s = 159{,}907$ W/m^2, (d) $q''_s = 238{,}524$ W/m^2, (e) $q''_s = 280{,}798$ W/m^2, and (f) flow images showing axial variation of flow patterns at heat flux $q''_s = 238{,}524$ W/m^2.

reaches a constant value associated with thermally fully developed conditions. After the first nucleation occurs at the ONB location, the transition of heat transfer mechanism from single-phase convection to subcooled flow boiling gradually takes place. When a single bubble is generated, the surface heat transfer is enhanced by the latent and sensible heat transfers associated with phase change and bubble agitation motions, respectively. As the flow regime transitions from PDB to FDB, nucleate boiling heat transfer becomes dominant over single-phase convection.

The surface heat flux, q''_s, affects the axial variation of the heat transfer mechanism as shown in Fig. 8. Fig. 8(a) illustrates the axial

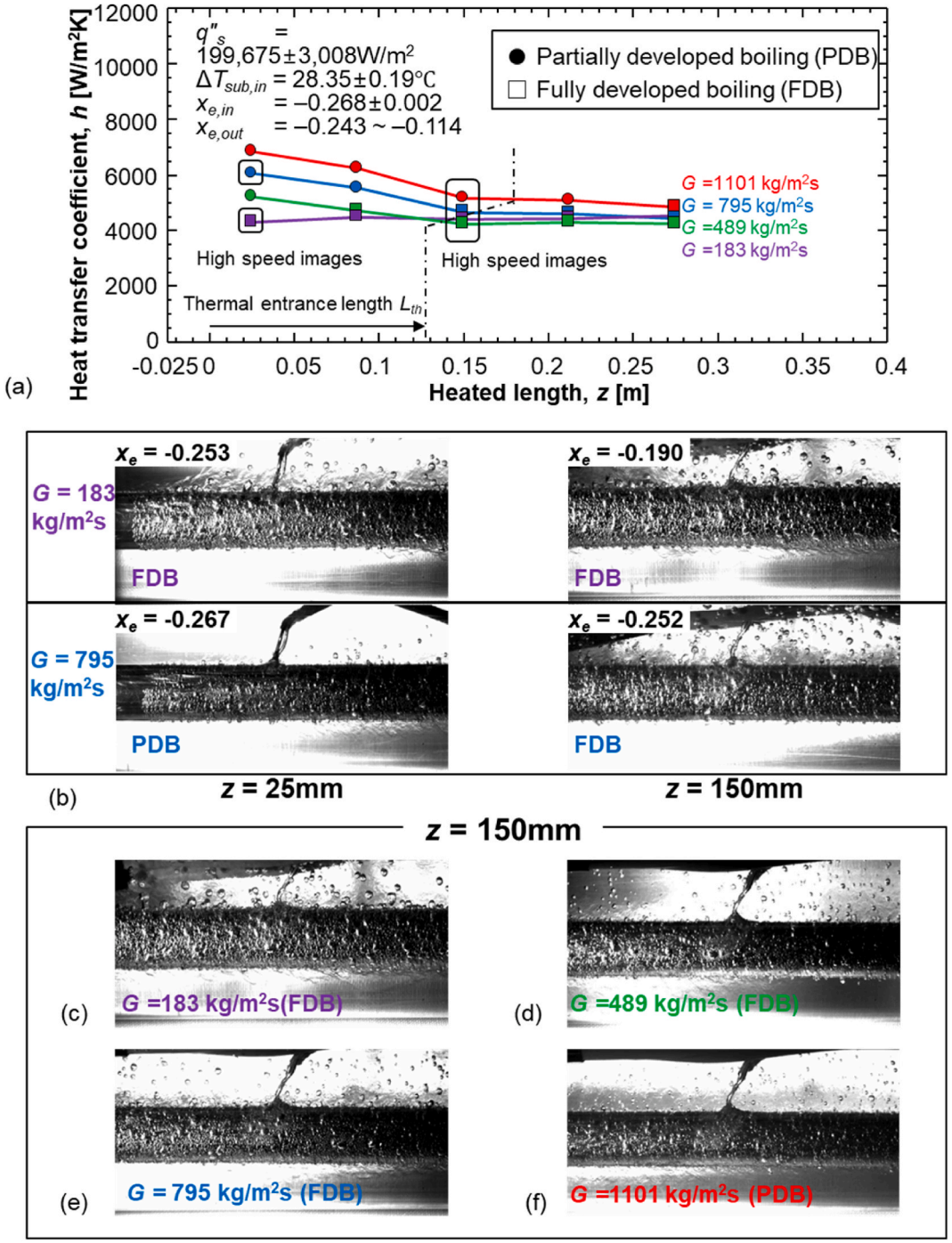

Fig. 9. (a) Axial variations of the experimental heat transfer coefficient, h, on the inner heating surface for subcooled flow boiling in concentric annuli with varying mass flux, G, as a function of heated length z. (b) Flow images comparing at $z = 25$ mm and $z = 150$ mm for $G = 183$ kg/m^{2}s, and 795 kg/m^{2}s. Flow visualization images at $z = 150$ mm with mass flux of (c) $G = 183$ kg/m^{2}s, (d) $G = 489$ kg/m^{2}s, (e) $G = 795$ kg/m^{2}s, and (f) $G = 1101$ kg/m^{2}s.

variations of the local heat transfer coefficient, h, for subcooled flow boiling at various heat fluxes, q''_s. The h value proportionally increases as q''_s increases at all five axial locations. Evidenced by the heat flux effect on the heat transfer coefficient, the nucleate boiling is considered the dominant heat transfer mechanism across the entire heated domain. The impact of heat flux on the flow regime is illustrated by flow images at $z_3 = 150.0$ mm with different heat fluxes, $q''_s = 79{,}452$ to $280{,}798$ W/m^2, as depicted in Fig. 8(b)–(e). As the heat flux increases, more nucleate bubbles are activated with increased surface superheat. Compared to the other three images of FDB, the PDB image at $q''_s = 79{,}452$ W/m^2 shows the single-phase flow characteristics, except for micro-sized bubbles sliding along the heated surface. The transition location from PDB to FDB shifts to the upstream region as q''_s increases because more nucleation sites are activated by increased surface superheat, ΔT_{sat}. This shift makes the FDB regime appears even in thermally developing region. For the highest heat flux condition $q''_s = 280{,}798$ W/m^2, the FDB regime appears from the heated length starting location, $z_1 = 25.0$ mm. An

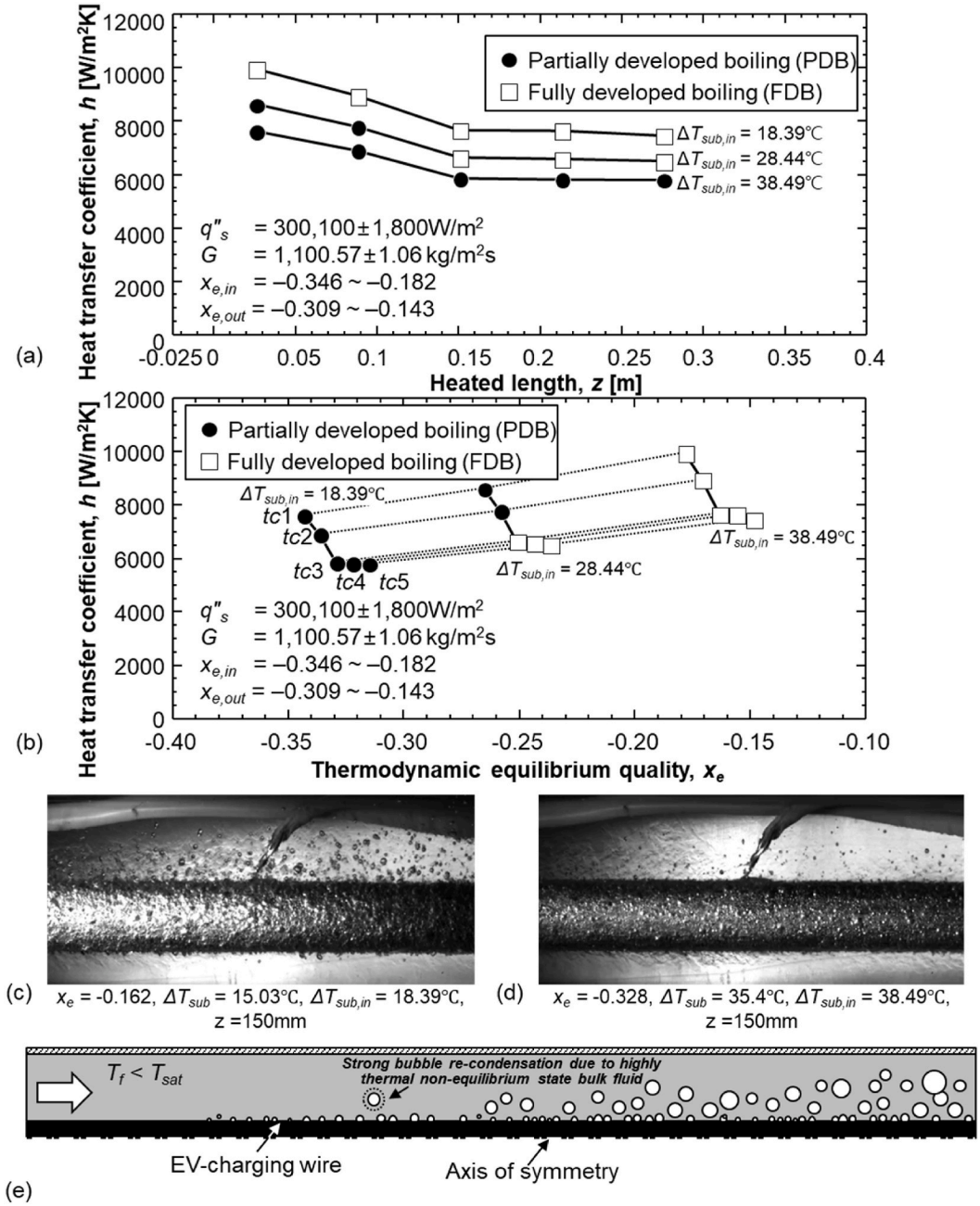

Fig. 10. Axial variations of the experimental heat transfer coefficient, h, on the inner heating surface for subcooled flow boiling in concentric annuli with varying inlet subcooling $\Delta T_{sub,in}$ according to the changes in (a) heated length z, (b) thermodynamic equilibrium quality x_e. Flow visualization images at $z = 150$ mm with inlet subcooling of (c) $\Delta T_{sub,in} = 18.39$ °C, and (d) $\Delta T_{sub,in} = 38.49$ °C. (e) Schematic of condensation effect in subcooled flow boiling.

interesting trend is observed where the heat transfer coefficient of FDB is influenced by thermal boundary layer development, which is assumed to be caused by the combined phenomena of thermal boundary layer and subcooled flow boiling that increase the level of thermal non-equilibrium state. These two phenomena enhance the thermal non-equilibrium state within the cross-section with the increase in the amount of subcooling. Although a few data points in the thermal entrance region are categorized into the FDB regime, they exhibit characteristics of the PDB regime, as shown in Fig. 8(a). Under strong single-phase convection effects in the thermal entrance region, a reversal between the PDB at z_1 and the FDB at z_2 in heat transfer coefficient is observed at $q_s'' = 199{,}848$ and 238,524 W/m^2. Due to significant thermal entrance effects, data points sorted as FDB exhibit pronounced single-phase convection characteristics in axial variations of the heat transfer coefficient. The flow visualization images in Fig. 8(f) show the variation of FDB flow patterns along the channel at $q_s'' = 238{,}524$ W/m^2, and, compared to flows at z_3 and z_5, the flow at z_1 shows a clearly smaller population of nucleate bubbles, which is characteristics of the PDB regime. Based on the measured heat transfer coefficients and flow visualization results, there are two possible reasons for the unexpected thermal characteristics of subcooled flow boiling in the thermally developing region: failure of demarcation by Shah's criteria and strong recondensation effect. First, Shah's demarcation criteria are considered to overestimate the nucleate boiling effects and fail in demarcation by sorting a portion of PDB, under strong subcooling and recondensation effects, as FDB. The Shah correlation was validated for annular gap ranging from 4.3 mm to 6.6 mm, which does not encompass the annular gap of the current experimental test module, which is 7.825 mm. If the annular gap becomes larger, boiling can be suppressed by re-condensation through effective heat exchange between floating bubbles and the subcooled bulk liquid. Second, a portion of the surface area without cavities can be exposed to single-phase liquid and undergo single-phase convection due to strong recondensation, even if all cavities are already activated. This can lead to a strong influence of thermal boundary layer development on the heat transfer process. From the results, the FDB regime is unexpectedly observed to be affected by single-phase convection, which requires further investigation in future studies to reveal the dominant heat transfer mechanisms of subcooled flow boiling under thermally developing conditions. In light of the discrepancy observed in thermal characteristics, the validity of Shah's criteria for flows in concentric annuli needs to be reconsidered in the future study.

The mass flow rate effect is investigated in Fig. 9 with a fixed $q_s'' = 199{,}675$ W/m^2 but different $G = 183$ to 1101 kg/m^{2}s. The thermal entrance effect is only observed in three cases of higher mass velocities, $G = 489$–1101 kg/m^{2}s, where clear changes in the axial trend of the heat transfer coefficient are observed when the flow is thermally fully developed from z_3. The significant differences in heat transfer coefficients among three flow conditions observed at z_1 are not observed at z_5, which shows the axial transition of the dominant heat transfer mechanism from single-phase convection to nucleate boiling. The significant differences in heat transfer coefficients among the three flow conditions observed at z_1 are not present at z_5. This indicates an axial transition of the dominant heat transfer mechanism from single-phase convection to nucleate boiling. However, there are still differences in heat transfer coefficients among the three flow conditions at z_5, as shown in Fig. 9(a). Despite their small magnitude, these differences can be attributed to two possible reasons: the enhancement of single-phase convection heat transfer and the effects of bulk liquid temperature. Although the flows under three different conditions are classified as FDB, the increase in fluid velocity can improve single-phase convection on the heated surface where no cavities exist. In addition, the difference in local bulk fluid temperature can affect the heat transfer rate on the heated surface. At the highest mass velocity condition, with $G = 1101$ kg/m^{2}s, the lowest local bulk fluid temperature occurs at z_5, assuming the inlet temperature and heat supply remain equivalent. These observations imply that flows categorized as FDB still exhibit thermal characteristics of single-phase convection to some extent, which differs from the definition of FDB, where the flows are considered fully independent of bulk fluid. These discrepancies might stem from misclassification of Shah's criteria or structural characteristics of concentric annular, and further investigation is required in the future study.

A different trend is observed with the constant heat transfer coefficient at the lowest mass velocity case, $G = 183$ kg/m^{2}s, which exhibits the FDB regime throughout the entire channel from the upstream region z_1. Because the nucleate boiling and associated bubble motions dominate the heat transfer process in the FDB regime, the effect of thermal boundary layer development on h is limited in the lowest mass velocity case of $G = 183$ kg/m^{2}s. In Fig. 9(b), the flow visualization images at two different mass velocities of $G =$ 183 and 795 kg/m^{2}s at two different locations, z_1 and z_3, are compared to demonstrate the flow regime and dominant heat transfer mechanism effects on the axial variation of heat transfer coefficients. More noticeable differences in the bubble motions are observed between two images for $G = 795$ kg/m^{2}s compared to $G = 183$ kg/m^{2}s, demonstrating the flow regime effects on the heat transfer mechanisms. In the thermally developed region, the case with the highest mass velocity $G = 1101$ kg/m^{2}s shows the highest h values due to stronger single-phase convection effects. The strong single-phase convection effect at highest mass velocity is evidenced by a smaller number of bubbles with smaller volumes compared to the cases with lower mass velocities $G = 183$–795 kg/m^{2}s as shown in Fig. 9(c)–(f) at $z = 150$ mm. In Fig. 9(f), the strong recondensation suppresses the bubble growth, allowing the liquid flow motions to participate in the heat transfer process on the heated surface without bubble interference resulting in highest heat transfer coefficient.

The flow subcooling effect on the heat transfer coefficient is investigated in Fig. 10. The heat transfer coefficient decreases throughout the channel with an increase in subcooling, as shown in Fig. 10(a). Having almost similar single-phase convection heat transfer coefficient, $h_{sp,f}$, the differences in the nucleate boiling heat transfer coefficient, h_{nb}, result in different values of h which are expressed by

$$h = h_{sp,f} + h_{nb}. \tag{27}$$

With the decrease in surface temperature T_s, the number of activated cavities having higher available superheat,

$$T_f = T_w - \frac{q''}{k_f} r, \tag{28}$$

than the required superheat,

$$T_{SH} = T_{sat} + \frac{T_{sat} v_{fg}}{h_{fg}} \frac{2\sigma}{r}, \tag{29}$$

decreases resulting in the reduction of nucleate boiling intensity [43]. As described in Eq. (20), the ONB location shifts downstream with a decrease in T_f. In addition, after ONB, with the increasing thermal non-equilibrium effect, the heightened subcooling accelerates the recondensation of generated bubbles. This process removes the heat transfer prevention from populated bubbles and suppresses bubble growth on the heated surface. The degree of thermal equilibrium increases with x_e, which leads to enhancement of nucleate boiling and an early transition from PDB to FDB as shown in Fig. 10(b). With enhanced nucleate boiling, the heat transfer coefficient generally increases with x_e at the same locations. The FDB regime becomes predominant as x_e increases until it reaches '0'. The subcooling effect on the flow regime is presented with two different mass velocity cases in Fig. 10(c) and (d) at $z = 150$ mm. The thermal non-equilibrium becomes stronger as subcooling increases, enhancing the bubble recondensation and suppression of nucleate boiling. In addition, the axial variation of flow regime and heat transfer mechanism are schematically described in Fig. 10(e). The amount of subcooling decreases along the annulus as the fluid absorbs heat from the inner heating wire, which leads to axial reductions in the degree of thermal non-equilibrium and vapor recondensation. Along the channel, but still under subcooled flow conditions, when $x_e < 0$, reduced subcooling leads to quicker bubble expansion in the bulk flow and activates more nucleation sites with increased bulk fluid temperature.

3.4. Assessment of subcooled flow boiling correlations for heat transfer coefficient

After conducting a thorough literature review, no correlation was found for subcooled flow boiling of the dielectric fluid HFE-7100 in horizontal concentric annuli. In this study, an attempt is made to assess previous correlations listed in Table 7. A total of 8 correlations for subcooled flow boiling heat transfer coefficients are tabulated with remarks related to cross sections (annuli/circular tube/rectangular), flow directions (horizontal/vertical), working fluids, and materials of the heated surface. This assessment is necessary because verifying the accuracy of these correlations in the experimental module allows for their application in predicting the thermal management performance of actual electric vehicle charging cables (3–7m), and these correlations can also be applied to various cable thicknesses and cooling fluid operating conditions. As shown in Fig. 11, the assessed prediction accuracies of eight correlations are provided, including the mean absolute error,

$$MAE(\%) = \frac{1}{N} \sum \left[\frac{\left| h_{pred} - h_{\exp} \right|}{h_{\exp}} \times 100 \right], \tag{30}$$

and inliers of θ and ξ, respectively, representing the percentages of data points predicted within ±30% and ±50%. The data points are separated into PDB and FDB and demarcated by solid and open symbols, respectively, with individual MAE (%) to assess the prediction accuracy of correlations for two different flow regimes. The standard deviation of the predicted heat transfer coefficient is given by

$$\sigma = \sqrt{\frac{1}{N-1} \sum_{n=1}^{N} \left(h_{pred,n} - \overline{h}_{pred} \right)^2}, \tag{31}$$

where $\overline{h}_{pred}$ represents the average of the predicted heat transfer coefficient of the data points. Most of the data is under-predicted by Papell's [44] correlation, with a MAE of 57.05 %, as shown in Fig. 11(a). Papell's correlation was developed for distilled water flowing in an Inconel X-resistant heated tube and has shown its extended applicability to liquid ammonia across a wide range of operating conditions. This under-prediction trend is assumed to be caused by its narrow applicable range, which only includes two working fluids in correlation development and validation. It is confirmed that the density ratio, ρ_g/ρ_f, of HEF-7100 is much higher than that of the other two fluids. Badiuzzaman's correlation [45], which has a similar form to Papell's but is based on three different fluids (distilled water, ethanol (95 %), and isopropanol) on a flat plate, secured a wider range of thermophysical properties and succeeded in prediction with a MAE of 13.99 %, as shown in Fig. 11(b). In addition, the tuning constant for organic fluid attributes to the high prediction accuracy of Badiuzzaman's correlation. However, the prediction trend changes depending on the flow regimes, with under-prediction for PDB and over-prediction for FDB. These discrepancies in prediction trends may arise from the differing thermophysical properties of the working fluids between the current experiments and the correlation's database, as ethanol and isopropanol have significantly higher specific heat C_p and latent heat of vaporization h_{fg} compared to HFE-7100 Compared to high prediction accuracy, a relatively lower level of precision is observed.

Compared to the aforementioned correlations, the correlation by Moles and Shaw [46] covers a wider range of operating conditions by incorporating 10 different sources and utilizing the Sieder-Tate equation [47]. The thermal entrance effect is reflected in the Sieder-Tate equation by considering the length and size of the test module. This correlation covers similar flow characteristics, such as horizontal flow and turbulent/macro-scale circular upward flow, as in the present study, but it does not consider dielectric fluids, as outlined in Table 6. The Moles and Shaw correlation overestimated the experimental heat transfer coefficients in both the PDB and FDB regimes, with a MAE of 24.62 % as shown in Fig. 11(c). It should be noted that the Mole and Shaw correlation showed the best prediction accuracy in one of the present authors' previous studies [12]. This discrepancy in prediction accuracy can be attributed to the different measurement locations in the circumferential direction. The top surface temperature is measured in the present study as shown in Fig. 3(d), while the side surface temperature was measured in one of present authors' previous study. The difference in

Table 7
Subcooled flow boiling correlations for heat transfer coefficient.

Author(s)	Correlations	Remarks
Papell (1963) [44]	$\frac{Nu_{sc}}{Nu_{sp}} = 90\left(\frac{q''_s}{h_{fg}\rho_g U}\right)^{0.7}\left(\frac{h_{fg}}{c_{p,f}\Delta T_{sub}}\right)^{0.84}\left(\frac{\rho_g}{\rho_f}\right)^{0.756}$ $= 90Bo^{0.7}Ja^{**-0.84}\left(\rho_g/\rho_f\right)^{0.056}$ $Nu_{sp} = 0.021\mathrm{Re}_f^{0.8}\mathrm{Pr}_f^{0.4}$	Cross sections: circular Flow directions: horizontal[a] Working fluids: distilled water, ammonia Materials: Inconel X tube MAE: 57.05 %
Badiuzzaman (1967) [45]	$\frac{Nu_{sc}}{Nu_{sp}} = C\left\{\left(\frac{q''_s}{h_{fg}\rho_g U}\right)\left(\frac{h_{fg}}{c_{p,f}\Delta T_{sub}}\right)^{1.2}\left(\frac{\rho_g}{\rho_f}\right)^{1.08}\left(\frac{\Delta T_{sub}}{T_{sat}}\right)^{0.6}\right\}^m$ $= C\left\{BoJa^{**-1.2}\left(\rho_g/\rho_f\right)^{0.08}\left(\Delta T_{sub}/T_{sat}\right)^{0.6}\right\}^m$ Water: $C = 178$, $m = 0.75$ Organic fluids: $C = 759$, $m = 0.89$ (used in this study) $Nu_{sp} = 0.021\mathrm{Re}_f^{0.8}\mathrm{Pr}_f^{0.4}$	Cross sections: rectangular Flow directions: horizontal[a] Working fluids: water, ethanol, and isopropanol Materials: stainless steel[a] MAE: 13.99 %
Moles and Shaw (1972) [46]	$\frac{Nu_{sc}}{Nu_{sp}} = 78.5\left(\frac{q''_s}{h_{fg}\rho_g U}\right)^{0.67}\left(\frac{h_{fg}}{c_{p,f}\Delta T_{sub}}\right)^{0.5}\left(\frac{\rho_g}{\rho_f}\right)^{0.7}\left(\frac{c_{p,f}\mu_f}{k_f}\right)^{0.46}$ $= 78.5Bo^{0.67}Ja^{**-0.5}\left(\rho_g/\rho_f\right)^{0.03}\mathrm{Pr}_f^{0.46}$ $Nu_{sp} = 0.027\mathrm{Re}_f^{0.8}\mathrm{Pr}_f^{1/3}\left(\frac{\mu_f}{\mu_f\big\vert_{T_s}}\right)^{0.14}\left(1+\left(\frac{D_h}{L_h}\right)^{0.7}\right)$ for $\frac{L_h}{D_h} < 60$	Cross sections: circular, rectangular Flow directions: horizontal[a], vertical up Working fluids: water, ethanol, isopropanol, n-butanol, ammonia, aniline, and hydrazine Materials: stainless steel[a], Inconel X, and nickel L and A MAE: 24.62 %
Shaw (1972) [47]	$\frac{Nu_{sc}}{Nu_{sp}} = 82\left(\frac{q''_s}{h_{fg}\rho_g U}\right)^{0.68}\left(\frac{h_{fg}}{c_{p,f}\Delta T_{sub}}\right)^{0.5}\left(\frac{\rho_g}{\rho_f}\right)^{0.69}\left(\frac{c_{p,f}\mu_f}{k_f}\right)^{0.46}$ $= 82Bo^{0.68}Ja^{**-0.5}\left(\rho_g/\rho_f\right)^{0.01}\mathrm{Pr}_f^{0.46}$ $Nu_{sp} = 0.027\mathrm{Re}_f^{0.8}\mathrm{Pr}_f^{1/3}\left(\frac{\mu_f}{\mu_f\big\vert_{T_s}}\right)^{0.14}\left(1+\left(\frac{D_h}{L_h}\right)^{0.7}\right)$ for $\frac{L_h}{D_h} < 60$	Operating conditions: Same as Moles and Shaw (1972) Cross sections: circular, rectangular, square annuli Flow directions: horizontal[a], vertical up Working fluids: water, ethanol, isopropanol, n-butanol, ammonia, aniline, and hydrazine Materials: stainless steel[a], Inconel X, and nickel L and A MAE: 34.12 %
Shah (1983) [48]	$q''_s = h_{sc}\left(T_s - T_f\right) = \begin{cases}\left(\psi_0 + \frac{\Delta T_{sub}}{\Delta T_{sat}}\right)h_{sp}\Delta T_{sat}, PDB \\ \psi_0 h_{sp}\Delta T_{sat}, FDB\end{cases}$ $\psi_0 = \begin{cases}230Bo^{0.5}, Bo > 0.2954\times10^{-4} \\ 1+46Bo^{0.5}, Bo < 0.2954\times10^{-4}\end{cases}$ $\frac{h_{sp}D_e}{k_f} = Nu_{sp} = 0.023\mathrm{Re}_f^{0.8}\mathrm{Pr}_f^{0.4}$ PDB (high subcooling): $\frac{\Delta T_{sub}}{\Delta T_{sat}} = \frac{T_{sat}-T_f}{T_s-T_{sat}} > 2$ or $\frac{\Delta T_{sub}}{\Delta T_{sat}} > 6.3\times10^4 Bo^{1.25}$ FDB (low subcooling): $\frac{\Delta T_{sub}}{\Delta T_{sat}} \le 2$ and $\frac{\Delta T_{sub}}{\Delta T_{sat}} \le 6.3\times10^4 Bo^{1.25}$	Cross sections: annuli[a], circular Flow directions: horizontal[a], vertical up Working fluids: water, R-113, Methanol, R-113, R-12, n-butyl alcohol, solutions of potassium carbonate, R-22, and cyclohexane Materials: copper, stainless steel[a], nickel, Inconel, and glass MAE: 16.11 %
Gungor and Winterton (1986) [49]	$q''_s = h_{sp}\left(T_s - T_f\right) + Sh_{nb}\left(T_s - T_{sat}\right) = h_{sc}\left(T_s - T_f\right)$ $\Rightarrow h_{sc} = h_{sp} + Sh_{nb}\frac{\Delta T_{sat}}{\left(T_s - T_f\right)}$ $\frac{h_{sp}D}{k_f} = Nu_{sp} = 0.023\mathrm{Re}_f^{0.8}\mathrm{Pr}_f^{0.4}$ $h_{nb} = 55P_R^{0.12}\left(-\log_{10}P_R\right)^{-0.55}M_W^{-0.5}q''^{\,0.67}_s$ $E = 1$ $S = \left(1+1.15\times10^{-6}E^2\mathrm{Re}_f^{1.17}\right)^{-1}$ For horizontal tubes and $Fr_f \le 0.05$, $E = EFr_f^{0.1-2Fr_f}$ and $S = SFr_f^{0.5}$ $Fr_f = \frac{G^2}{\rho_f^2 g D_h} = \frac{U^2}{gD_h}$	Cross sections: annuli[a], circular Flow directions: horizontal[a], vertical Working fluids: water, refrigerants, and ethylene glycol Materials: stainless steel[a], Inconel X MAE: 26.66 %
Liu & Winterton (1991) [50]	$q''_s = \left(\left(Eh_{sp}\left(T_s - T_f\right)\right)^2 + \left(Sh_{nb}\Delta T_{sat}\right)^2\right)^{0.5} = h_{sc}\left(T_s - T_f\right)$ $\Rightarrow h_{sc} = \left(\left(Eh_{sp}\right)^2 + \left(Sh_{nb}\frac{\Delta T_{sat}}{\left(T_s - T_f\right)}\right)^2\right)^{0.5}\frac{h_{sp}D}{k_f} = Nu_{sp} =$ $0.023\mathrm{Re}_f^{0.8}\mathrm{Pr}_f^{0.4}$ $h_{nb} = 55P_R^{0.12}\left(-\log_{10}P_R\right)^{-0.55}M_W^{-0.5}q''^{\,0.67}_s$ $E = 1$ $S = \left(1+0.055E^{0.1}\mathrm{Re}_f^{0.16}\right)^{-1}$ For horizontal tubes and $Fr_f \le 0.05$, $E = EFr_f^{0.1-2Fr_f}$ and $S = SFr_f^{0.5}$ $Fr_f = \frac{G^2}{\rho_f^2 g D_h} = \frac{U^2}{gD_h}$	Cross sections: annuli[a], circular Flow directions: horizontal[a], vertical Working fluids: water, refrigerants, ethylene glycol, ethanol, and n-butanol Materials: stainless steel[a], Inconel X MAE: 35.38 %

(*continued on next page*)

Table 7 (*continued*)

Author(s)	Correlations	Remarks
Shah (2017) [51]	$q''_s = h_{sc}(T_s - T_f) = \begin{cases} \dfrac{\psi_0 h_{sp}(\Delta T_{sat} - 1.65\Delta T_{sub}^{-0.44})}{0.67}, PDB \\ \psi_0 h_{sp} \Delta T_{sat}, FDB \end{cases}$ $\psi_0 = \begin{cases} 230Bo^{0.5}, Bo > 0.2954 \times 10^{-4} \\ 1 + 46Bo^{0.5}, Bo < 0.2954 \times 10^{-4} \end{cases}$ $\frac{h_{sp}D}{k_f} = Nu_{sp} = 0.023\mathrm{Re}_f^{0.8}\mathrm{Pr}_f^{0.4}$ PDB (high subcooling): $\frac{\Delta T_{sub}}{\Delta T_{sat}} = \frac{T_{sat} - T_f}{T_s - T_{sat}} > 2$ or $\frac{\Delta T_{sub}}{\Delta T_{sat}} > 6.3 \times 10^4 Bo^{1.25}$ FDB (low subcooling): $\frac{\Delta T_{sub}}{\Delta T_{sat}} \le 2$ and $\frac{\Delta T_{sub}}{\Delta T_{sat}} \le 6.3 \times 10^4 Bo^{1.25}$	Cross sections: annuli[a], circular, rectangular Flow directions: horizontal[a], vertical Working fluids: water, ammonia, R-11, R-12, R-113, R-123, R-134a, FC-72, HFE-7100[a], isopropanol, hexane, cyclohexane, and methanol Materials: stainless steel[a], copper, brass, zirconium-copper alloy, nickel, Inconel, and glass MAE: 13.94 %

[a] Matched with the current experimental conditions (cross section: annuli, flow direction: horizontal, working fluid: HFE-7100, material: stainless steel.).

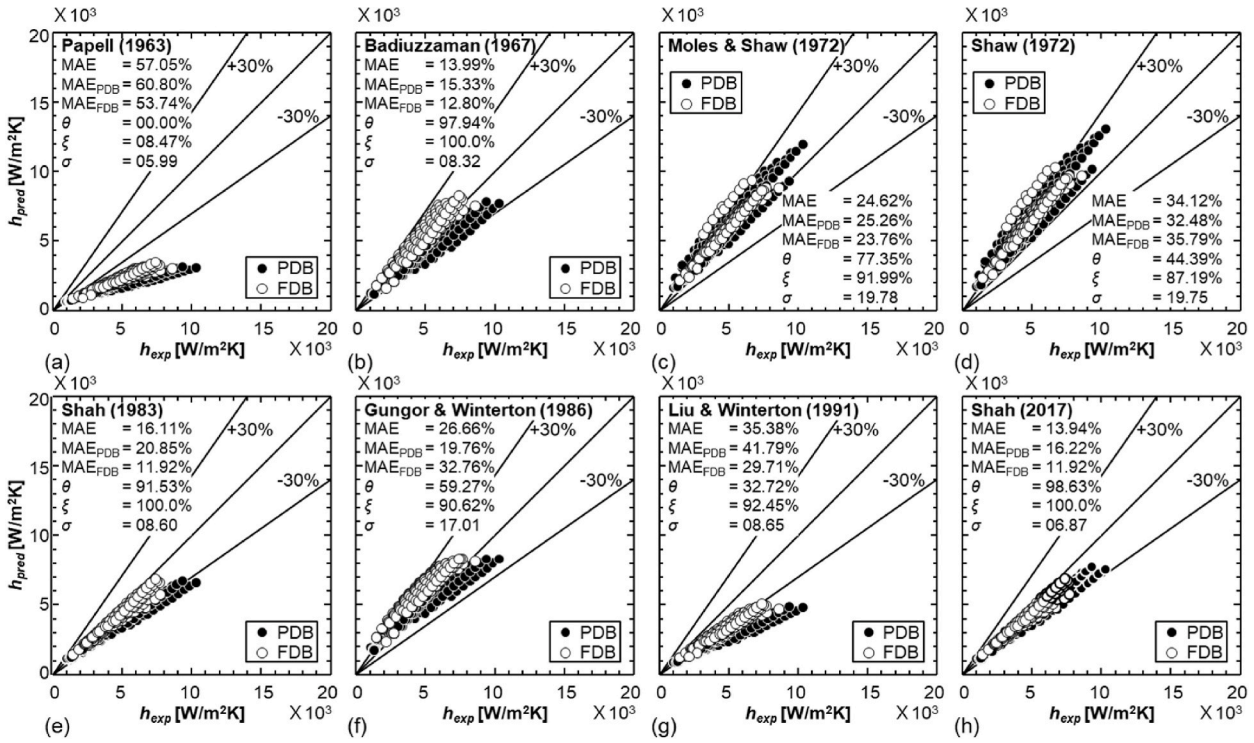

Fig. 11. Comparison of experimental data to predictions by previous correlations for the heat transfer coefficient of subcooled flow boiling: (a) Papell (1963), (b) Badiuzzaman (1967), (c) Moles and Shaw (1972), (d) Shaw (1972), (e) Shah (1983), (f) Gungor and Winterton (1986), (g) Liu and Winterton (1991), and (h) Shah (2017).

measurement location influences heat transfer results due to the enhanced heat transfer coefficient resulting from the sliding motion of bubbles along a circular heated surface. The highest heat transfer coefficient is typically observed at the side under flow boiling conditions [52]. As shown in the flow visualization results in Fig. 12, the top surface is considered to have a higher surface temperature due to the increased fluid temperature induced by the recondensation of accumulated bubbles. The smaller bubbles generated at the bottom and side surfaces slide along the circumferential direction and accumulate into larger bubbles on the top surface due to the buoyancy force, creating thermal non-equilibrium in the bulk flow cross-section. Detailed investigation into the asymmetric thermal characteristics along the circumferential direction induced by non-uniform bubble accumulation needs to be conducted in the future studies.

The Shaw [53] correlation was developed by modifying Moles and Shaw's [46] correlation, incorporating subcooled flow boiling data of water flowing through concentric annuli with a circular tube at the center of a squared outer tube. However, it overpredicts data with a MAE of 34.12 %, which is higher than the original correlation because the additionally added fluids exhibit different thermophysical properties compared to HFE-7100. Developed based on 883 data collected from 11 sources those cover a wide range of operating conditions, Shah (1983) [48] correlation showed a high prediction accuracy with a MAE of 16.11 %, as shown in Fig. 11(e).

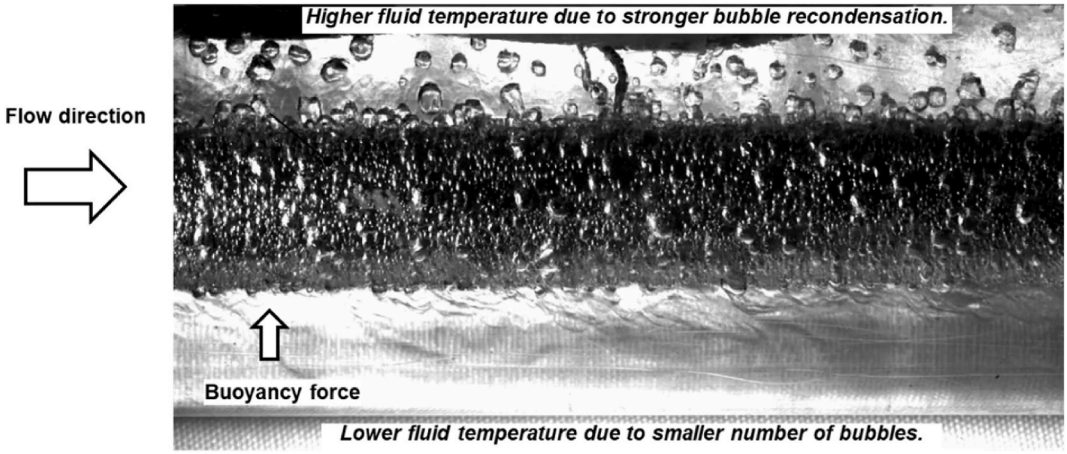

Fig. 12. Effect of buoyancy force on thermal non-equilibrium of fluid in concentric annuli. Flow visualization image representing accumulated bubbles on top of the test module at TC5.

Having different equations for each flow regime, the correlation still shows varying prediction accuracies for PDB and FDB, with MAEs of 20.85 % and 11.92 %, respectively. The reason why the experimental heat transfer coefficient was under-predicted in the PDB regime is that the current experimental heat transfer coefficients were enhanced by the thermal entrance effect, which was not accounted for in Shah's correlation. Both Gungor and Winterton (1986) [49] and Liu and Winterton (1991) [51] correlations are based on the same database, which includes various flow configurations and fluids, but they exhibited different prediction accuracies of MAEs of 26.66 % and 35.38 %, respectively, as illustrated in Fig. 11(f) and (g). Liu and Winterton utilized the bulk fluid temperature to calculate the liquid Prandtl and Reynolds numbers, Pr_f and Re_f, to enhance the accuracy of their experimental data. This change is suspected to be the one of reasons for the under-prediction associated with the reduced intensity of the nucleate boiling. A reduced suppression factor S affecting the nucleate boiling heat transfer coefficient leads to different predictions compared to Gungor and Winterton. Shah (2017) [51], a modified version of the correlation developed by Shah (1983) [48], demonstrated the best predictive

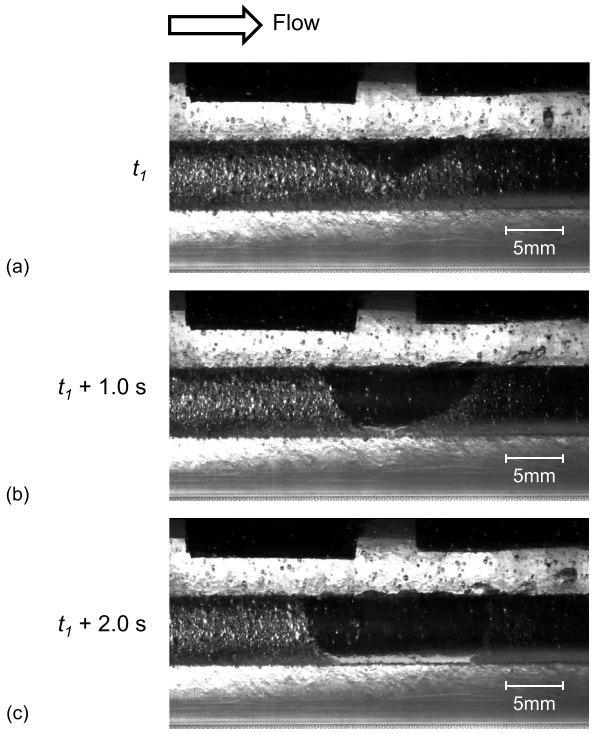

Fig. 13. High-speed video images capture the triggering instant and propagation of DNB-type CHF occurring on the inner heated surface of concentric annuli at a mass flux of $G = 947.91$ kg/m^{2}s, inlet fluid temperature $T_{in} = 20$ °C, critical heat flux $q''_{CHF} = 420{,}000$ W/m^2, and module inlet pressure $P_{in} = 212.34$ kPa. The time interval between consecutive images is set to 1.0 s.

accuracy with a MAE of 13.94 %, attributed to its database enriched with various flow configurations and the corresponding adjustments made to its equations. The method for estimating the heat flux in the PDB regime has been updated to an empirical correlation tailored to a new database, with adjustments made based on the boiling number, *Bo*, which demarcates the flow regimes between PDB and FDB. The database includes the flow configuration used in the present study, which involves the subcooled flow boiling of HFE-7100 in horizontal concentric annuli with annular gaps ranging from 0.5 to 11.4 mm, under inner surface heating conditions.

3.5. Critical heat flux

Accurately predicting the critical heat flux (CHF) during subcooled flow boiling is crucial for the thermal management of electric

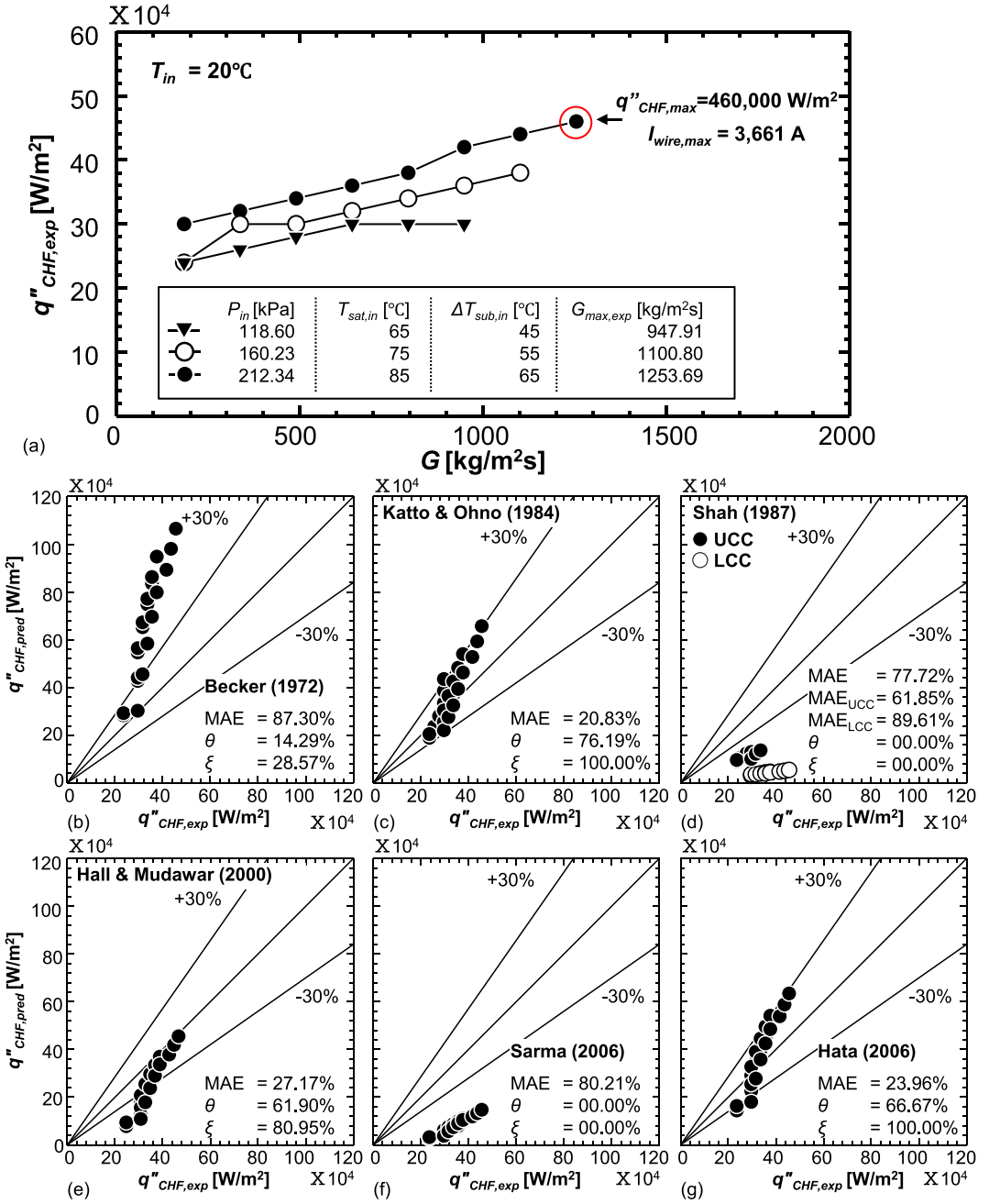

Fig. 14. (a) Variation of CHF with mass flux changes at different pressures (with different saturation temperatures) on the inner heated wall of concentric annuli, and comparison of the current CHF data with predictions by (b) Becker (1972), (c) Katto and Ohno (1984), (d) Shah (1987), (e) Hall and Mudawar (2000), (f) Sarma (2006), and (g) Hata (2006).

vehicle charging cables, as reaching CHF can cause a sudden rise in surface temperature due to the low thermal conductivity of the vapor, potentially leading to burnout of the charging system. In the high q''_s range, the DNB-type CHF occurs, which is manifested by a sudden increase in the surface temperature, T_{s5}, and the formation of a vapor blanket in the downstream region. It is noted that the CHF is initiated from the end of heated region, as shown in Fig. 13(a). The axial rise of fluid temperature diminishes the intensity of bubble recondensation, leading to the coalescence of populated small bubbles and the subsequent formation of a vapor blanket in the downstream region. It should be also noted that the vapor blanket initiates formation on the top side due to its relatively higher fluid temperature compared to the bottom side, and this asymmetric fluid temperature establishment is caused by the stronger recondensation of accumulated bubbles on the top side. The asymmetric bubble population is driven by buoyancy force that moves the bubbles from bottom to top side. The reduction in the heat transfer coefficient, h, leads to a local temperature increase and the propagation of the vapor blanket in the circumferential and longitudinal directions, as shown in Fig. 13(b) and (c). The circumferential propagation precedes the axial propagation as the surface temperature gradient in the axial direction is higher than in the circumferential direction. The velocity difference between two phases with different densities induces the Kelvin-Helmholtz instability, identified by a wavy interface as shown in Fig. 13(c). For the demonstration of the trigger mechanism and propagation of a vapor blanket, the high-speed video is provided in the supplementary data.

The mass flux effects on CHF are investigated at three different operating pressures, as shown in Fig. 14(a). With an increase in the heat transfer coefficient, h, the rise in mass flux reduces the surface superheat, leading to a decrease in the number of activated cavities. Due to the increased liquid inertia that sweeps away the accumulated bubbles on the heated surface, the increased mass flux generally enhances the CHF. However, the mass flux effects on CHF enhancement saturate when the bubble crowding effect becomes strong enough that the liquid inertia cannot prevent the vapor blanket formation and subsequent transition to CHF. This is observed in the case of $P_{in} = 118.60$ kPa where the CHF is saturated at $q''_{CHF} = 300{,}000$ W/m^2, and a similar phenomenon is expected to occur at higher pressures of $P_{in} = 160.23$ and 212.34 kPa with extended operating ranges of G and q''_s. At an inlet pressure of $P_{in} = 232.34$ kPa, the maximum mass flux achievable in the experiment is $G_{\max} = 1253.69$ kg/m^{2}s, with a corresponding critical heat flux of $q''_{CHF} = 460{,}000$ W/m^2. When converted to charging current, this equates to $I_{\text{wire}} = 3661$ A, which is more than seven times the current used in typical fast chargers (500 A). This significant increase in charging current suggests that subcooled flow boiling could play an important role in managing the thermal load of EV charging cables and enhancing thermal management in other industrial applications, such as nuclear reactor cooling systems and double-pipe heat exchangers that use concentric annuli. The principles explored in this study may also be applicable to other thermal management challenges, such as those in Polymer Electrolyte Membrane (PEM) fuel cells, offering potential guidelines for optimizing design and safety. The saturation of CHF was not observed for two higher pressures within $G_{\max,exp}$ and $q''_{\max}$. The operating pressure also increases the CHF by reducing superheat, ΔT_{sat}, and increasing subcooling, ΔT_{sub}. The reduced superheating induced by increased pressure causes a reduction in the number of activated cavities, while increased subcooling enhances the recondensation phenomena. With the decrease of x_e, the enhanced thermal non-equilibrium state accelerates the recondensation phenomena. Reduction in nucleate boiling and enhanced recondensation together prevent the formation of a vapor blanket and increase the CHF.

Six different correlations have been assessed for their accuracies in predicting 21 experimental CHF data as shown in Fig. 14(b)–(g), and the information, along with detailed descriptions of their special features, is provided in Table 8. In the descriptions, the CHF correlations were classified into two types: inlet (upstream) conditions and outlet (local) condition correlations [16]. The MAE for CHF is defined as

$$MAE(\%) = \frac{1}{N}\sum\left[\frac{\left|q''_{CHF,pred} - q''_{CHF,\exp}\right|}{q''_{CHF,\exp}} \times 100\right]. \tag{32}$$

The correlation by Becker et al. [17] over-predicts with a MAE of 87.30 % due to significant differences in flow configurations and thermophysical properties, as outlined in Table 8. The primary reason for the over-prediction is attributed to water's superior thermophysical properties compared to the dielectric fluid, HFE-7100, and the extremely high operating pressure that causes significantly high subcooling. Recommended application ranges of this correlation are mass velocity of $G = 2000$–7000 kg/m^{2}s and system pressure of $P = 12{,}000$–$20{,}000$ kPa. These ranges are very different from the present study's experimental conditions, $G = 183.47$–1406.58 kg/m^{2}s and $P_{in} = 118.45$–212.34 kPa, and these differences caused errors in the predictions. The correlation by Katto and Ohno [18] exhibited the best prediction accuracy with a MAE of 20.83 % as illustrated in Fig. 14(c). This correlation can account for the differences in thermophysical properties among various working fluids, as it is developed based on multiple working fluids in the database. In addition, the present study's operating conditions, with $L/D_h = 19.2$ and $\rho_g/\rho_f = 0.00137$, fall within the applicable range of correlation, where $5 < L/D_h < 880$ and $0.0003 < \rho_g/\rho_f < 0.41$. The correlation by Shah (1987) [19] was developed using 23 different fluids from 62 sources of vertical upflow in uniformly heated tubes. The unique feature of this correlation is employing different relations depending on operating conditions: upstream condition correlation (UCC) and local condition correlation (LCC). UCC is used when CHF depends on inlet subcooling and distance from the tube inlet, while LCC is used when the CHF depends on the local quality, except for very short tubes. The Y parameter was used to distinguish between two correlations of CHF conditions, and the current database is divided by $G = 489.24$kg/m^{2}s according to Y parameter. As shown in Fig. 14(d), 12 out of 21 CHF data points are sorted into LCC data. The poor prediction accuracy is evident with MAE of 77.72 %, with 61.85 % for UCC data and 89.61 % for LCC data. It should be noted that the data sorted into LCC prediction showed a higher MAE of 89.61 %, even though all CHF data in this study are identified to occur by the same mechanism of DNB. Correlation by Hall and Mudawar [16] was developed based on 4860 data for CHF of subcooled water flows in uniformly heated tubes. This correlation consists of two sub-correlations, which are based on inlet and

Table 8
Critical heat flux correlations.

Author(s)	Correlation	Remarks
Becker (1972) [17]	$q''_{CHF} = \frac{G(450 + (h_f - h_{in}))}{40\frac{L_h}{D_h} + 156G^{0.45}}(1.02 - (P_R - 0.54)^2)$ G: kg/m^{2}s, h: kJ/kg, q''_{CHF}: W/cm^2	Inlet condition Cross sections: circular tube Flow directions: vertical up flow Working fluids: water MAE: 87.30 %
Katto and Ohno (1984) [18]	$q''_{CHF} = q''_{CHF,x_{e,in}=0}\left(1 + K\frac{h_f - h_{in}}{h_{fg}}\right)$ If $\rho_g/\rho_f < 0.15$: $q''_{CHF,x_{e,in}=0} = \begin{cases} q''_{co,1}, q''_{co,1} \le q''_{co,2} \\ \min\left\{q''_{co,2}, q''_{co,3}\right\}, q''_{co,1} > q''_{co,2} \end{cases}$ $K = \max\{K_1, K_2\}$ If $\rho_g/\rho_f > 0.15$: $q''_{CHF,x_{e,in}=0} = \begin{cases} q''_{co,1}, q''_{co,1} \le q''_{co,5} \\ \max\left\{q''_{co,4}, q''_{co,5}\right\}, q''_{co,1} > q''_{co,5} \end{cases}$ $K = \begin{cases} K_1, K_1 > K_2 \\ \min\{K_2, K_3\}, K_1 < K_2 \end{cases}$ $\frac{q''_{co,1}}{Gh_{fg}} = CWe_f^{-0.043}\frac{D_h}{L_h}$ $\frac{q''_{co,2}}{Gh_{fg}} = 0.10\left(\frac{\rho_g}{\rho_f}\right)^{0.133} We_L^{-\frac{1}{3}}\frac{1}{1 + 0.0031\frac{L_h}{D_h}}$ $\frac{q''_{co,3}}{Gh_{fg}} = 0.098\left(\frac{\rho_g}{\rho_f}\right)^{0.133} We_L^{-0.433}\frac{\left(\frac{L_h}{D_h}\right)^{0.27}}{1 + 0.0031\frac{L_h}{D_h}}$ $\frac{q''_{co,4}}{Gh_{fg}} = 0.0384\left(\frac{\rho_g}{\rho_f}\right)^{0.6} We_L^{-0.173}\frac{1}{1 + 0.28We_L^{-0.233}\frac{L_h}{D_h}}$ $\frac{q''_{co,5}}{Gh_{fg}} = 0.234\left(\frac{\rho_g}{\rho_f}\right)^{0.513} We_L^{-0.433}\frac{\left(\frac{L_h}{D_h}\right)^{0.27}}{1 + 0.0031\frac{L_h}{D_h}}$ $C = \begin{cases} 0.25, L_h/D_h \le 50 \\ 0.25 + 0.0009\left(\frac{L_h}{D_h} - 50\right), 50 \le L_h/D_h \le 150 \\ 0.34, L_h/D_h > 150 \end{cases}$ $K_1 = \left(\frac{1.043}{4CWe_L^{-0.043}}\right)$ $K_2 = \left(\frac{5\left(0.0124 + \frac{D_h}{L_h}\right)}{6\left(\frac{\rho_g}{\rho_f}\right)^{0.133} We_L^{-\frac{1}{3}}}\right)$ $K_3 = 1.12\left(\frac{1.52We_L^{-0.233} + \frac{D_h}{L_h}}{\left(\frac{\rho_g}{\rho_f}\right)^{0.6} We_L^{-0.173}}\right)$	Inlet condition Cross sections: circular tube Flow directions: vertical up flow Working fluids: Water, anhydrous ammonia, benzene, ethanol, helium I, para-hydrogen, monoisopropylbiphenyl, nitrogen, potassium, R-12, R-21, R-22, R-113, R-114, R-115 MAE: 20.83 %
Shah (1987) [19]	$Y = \left(\frac{GD_hc_{p,f}}{k_f}\right)\left(\frac{G^2}{\rho_f^2 gD_h}\right)^{0.4}\left(\frac{\mu_f}{\mu_g}\right)^{0.6}$ For liquid helium, use Upstream Condition Correlation. For other fluids: $q''_{CHF} = \begin{cases} q''_{CHF,UCC}, Y \le 10^6 \\ q''_{CHF,UCC}, Y > 10^6 \& L_E > \frac{160}{P_r^{1.14}} \\ \min\left\{q''_{CHF,UCC}, q''_{CHF,LCC}\right\}, Y > 10^6 \& L_E \le \frac{160}{P_r^{1.14}} \end{cases}$ Upstream Condition Correlation (UCC): $\frac{q''_{CHF}}{Gh_{fg}} = 0.124\left(\frac{D_h}{L_E}\right)^{0.89}\left(\frac{10^4}{Y}\right)^n(1 - x_{e,in,E})$ $x_{e,in,E} = \begin{cases} x_{e,in}, x_{e,in} \le 0 \\ 0, x_{e,in} > 0 \end{cases}$ $L_E = \begin{cases} L_{CHF}, x_{e,in} \le 0 \\ L_B, x_{e,in} > 0 \end{cases}$	Inlet condition (UCC), outlet condition (LCC) Cross sections: circular tube Flow directions: vertical up flow Working fluids: Water, R-11, R-12, R-21, R-22, R-113, R-114, ammonia, hydrazine, N2O4, MIPD, CO2, helium, nitrogen, hydrogen, acetone, benzene, diphenyl, ethanol, ethylene glycol, o-terphenyl, potassium, rubidium MAE: 77.72 %

(*continued on next page*)

Table 8 (*continued*)

Author(s)	Correlation	Remarks
	For liquid helium, $n = \left(\frac{D_h}{L_E}\right)^{0.33}$ For other fluids: $n = \begin{cases} 0, Y \le 10^4 \\ \left(\frac{D_h}{L_E}\right)^{0.33}, Y > 10^4 \\ \left(\frac{D_h}{L_E}\right)^{0.54}, 10^4 < Y \le 10^6 \\ \frac{0.12}{\left(1-x_{e,in,E}\right)^{0.5}}, Y > 10^6 \end{cases}$ $\frac{L_B}{D_h} = \frac{x_{e,CHF}}{4Bo} = \frac{L_{CHF}}{D_h} + \frac{x_{e,in}}{4Bo}$ Local Condition Correlation (LCC): $\frac{q''_{CHF,LCC}}{Gh_{fg}} = F_E F_x Bo_{x_{e,CHF}=0}$ $F_E = \max\left\{1, 1.54 - 0.032\left(\frac{L_{CHF}}{D_h}\right)\right\}$ $Bo_{x_{e,CHF}=0} = \max\left\{\begin{matrix} 15Y^{-0.612}, \\ 0.082Y^{-0.3}\left(1+1.45P_r^{4.03}\right), \\ 0.0024Y^{-0.105}\left(1+1.15P_r^{3.39}\right) \end{matrix}\right\}$ For $x_{e,CHF} > 0$, $F_x = F_3\left[1 + \frac{\left(F_3^{-0.29}-1\right)\left(P_r-0.6\right)}{0.35}\right]^c$ $c = \begin{cases} 0, P_R \le 0.6 \\ 1, P_R > 0.6 \end{cases}$ $F_3 = \left(\frac{1.25\times10^5}{Y}\right)^{0.833x_{e,CHF}}$ For $x_{e,CHF} < 0$, $F_x = F_1\left[1 - \frac{\left(1-F_2\right)\left(P_R-0.6\right)}{0.35}\right]^b$ $b = \begin{cases} 0, P_R \le 0.6 \\ 1, P_R > 0.6 \end{cases}$ $F_1 = 1 + 0.0052\left(-x_{e,CHF}^{0.88}\right)\left(\min\left\{1.4\times10^7, Y\right\}\right)^{0.41}$ $F_2 = \begin{cases} F_1^{-0.42}, F_1 \le 4 \\ 0.55, F_1 > 4 \end{cases}$	
Hall and Mudawar (2000) [16]	Based on outlet quality: $Bo_{CHF} = \frac{q''_{CHF}}{Gh_{fg}} = C_1 We_D^{C_2}\left(\frac{\rho_f}{\rho_g}\right)^{C_3}\left[1 - C_4\left(\frac{\rho_f}{\rho_g}\right)^{C_5} x_{e,out}\right]$ Based on pseudo-inlet quality (employed): $Bo_{CHF} = \frac{q''_{CHF}}{Gh_{fg}} = \frac{C_1 We_D^{C_2}\left(\frac{\rho_f}{\rho_g}\right)^{C_3}\left[1 - C_4\left(\frac{\rho_f}{\rho_g}\right)^{C_5} x^*_{e,in}\right]}{1 + 4C_1C_4 We_D^{C_2}\left(\frac{\rho_f}{\rho_g}\right)^{C_3+C_5}\left(\frac{L_h}{D_h}\right)}$ $x^*_{e,in} = \frac{h_{in} - h_{f,out}}{h_{fg,out}}$ $C_1 = 0.0722; C_2 = -0.312; C_3 = -0.644; C_4 = 0.900; C_5 = 0.724$	Outlet condition Cross sections: circular tube Flow directions: horizontal[a] flow, vertical up flow Working fluids: Water MAE: 27.17 %
Sarma et al. (2006) [20]	$Bo_{CHF} = \frac{q''_{CHF}}{Gh_{fg}} = 0.118\mathrm{Re}^{-0.23}P_R^{0.2}\left(\frac{D_h}{L_h}\right)^{0.45}\left(\frac{c_{p,f}\Delta T_{sub}}{h_{fg}}\right)$	Inlet condition Cross sections: circular tube Flow directions: not specifically oriented Working fluids: Water and R-12 MAE: 80.21 %
Hata (2006) [21]	$Bo_{CHF} = C_1\left(\frac{D_h}{\sqrt{\frac{\sigma}{g(\rho_f-\rho_g)}}}\right)^{-0.1} We_D^{-0.3}\left(\frac{L_h}{D_h}\right)^{-0.1} e^{\left(-\frac{L_h/D}{C_2\mathrm{Re}^{0.4}}\right)\left(\frac{c_{p,f}\Delta T_{sub,in}}{h_{fg}}\right)^{C_3}}$	Inlet condition Cross sections: circular tube Flow directions: vertical up flow Working fluids: Water MAE: 23.96 %

[a] Matched with the current experimental conditions (cross section: annuli, flow direction: horizontal, working fluid: HFE-7100).

outlet (local) conditions, respectively. The inlet conditions include diameter, heated length, mass velocity, pressure and inlet quality, and the correlation is recommended for water flow with uniform axial heat flux. While outlet conditions include diameter, mass velocity, pressure and outlet quality, and the correlation is applicable to water flow in a tube with a non-uniform axial heat flux condition. Inlet condition correlation can be obtained by transforming the outlet condition correlation using an energy balance between the inlet and outlet, and pseudo-inlet quality is introduced. CHF is predicted using inlet condition correlation because the current experimental heat flux conditions are uniform. This correlation slightly underpredicts the current experimental CHF data with MAE of 27.17 %, as depicted in Fig. 14(e). The underprediction becomes particularly noticeable in low G range. The flow rates tested in this study, ranging from G = 183.47–300 kg/m^{2}s, are not within the range covered by this correlation, which is G = 300–30,000 kg/m^{2}s. The correlation by Sarma et al. (2006) [20] was developed for DNB type CHF based on 3050 data points of flows in tubes with small diameters less than 3 mm at various pressures. It under-predicts the present CHF data with a MAE of 80.21 %, and poor prediction accuracy is attributed to differences in fluid thermophysical properties between the working fluid HFE-7100 and the fluids (water and R-12) used for correlation development. Based on 1805 data of vertical upflows of water in short-heated tubes, the correlation by Hata et al. [21] was developed for CHF of subcooled flow boiling in both short and large length-to-diameter tubes. This is the updated version of the previous correlation [54] for extended length to diameter ratio up to L/D = 75 on the 2 mm tube and for larger diameter tube with same L/d. It shows good prediction accuracy with MAE of 23.96 % as shown in Fig. 14(g) because this correlation included length to diameter ratio in the equation, which reasonably explains flow physics associated with CHF in current short length inner surface heating annulus.

3.6. Comparison of EV charging times: Estimation from laboratory-scale experiments vs. commercial chargers worldwide

Although this study is based on prototype experiments, comparing the results with existing commercial chargers worldwide is valuable, as it provides readers with practical insights relevant to reducing charging time. To prevent any misunderstanding, assumptions and differences from existing cable systems are clearly stated. Table 9 detailing the assumptions used in this study, including cable length, heat generation, concentricity, flow direction, and charging power consistency has been included. The bar chart in Fig. 15 demonstrates the time required to charge up to 80 % of a 100 kWh EV battery using the continuous charging method with various DC chargers available worldwide. While all fast chargers can theoretically charge within 15 min if the charging power is maintained at its maximum level throughout the entire charging period, they still take much longer than the conventional ICEV refueling time of 3 min. Commercial fast chargers typically use single-phase air or liquid cooling methods, which limit their charging speed. In one of authors' previous study [12], a 304.8 mm long horizontal concentric annuli were examined. The test module consisted of a uniformly heated inner surface and an adiabatic outer tube with respective diameters of 6.35 mm and 23.62 mm. The maximum heat flux and equivalent charging current were 199,210 W/m^2 and 2438 A, respectively. This reduced charging time by up to 2.4 min, assuming a charging voltage of 800 Vdc. The current experimental study involves a 300 mm long horizontal concentric annuli with a uniformly heated inner surface. The adiabatic outer tube diameters are 6.35 mm and 22 mm, respectively. The subcooled flow boiling cooling scheme can handle higher heat loads, up to 460,000 W/m^2, and a charging rate of up to 3661 A, constrained by CHF. This results in a reduced charging time by up to 1.6 min (98 s), which is expected to enhance consumer convenience and eliminate the inconvenience associated with charging issues.

4. Conclusions

This study explored thermal management strategies for electric vehicle charging cables using subcooled flow boiling of HFE-7100 in concentric annuli, leading to the following key findings.

(1) The proposed cooling method achieved a high heat flux of 460,000 W/m^2 under specific operating conditions, demonstrating the potential to supply a charging current of 3661 A, which is more than seven times the standard fast-charging current of 500 A. This experimentally proves that subcooled flow boiling is a highly promising method for the thermal management of future ultra-fast EV charging cables.
(2) Nucleate boiling was found to dominate the heat transfer mechanism, with single-phase convection having an impact only in the thermally developing region. Among the evaluated correlations, Shah's (2017) correlation [51] provided the most accurate predictions for the heat transfer coefficient, suggesting its applicability for predicting the thermal performance of commercial EV charging cables.
(3) The DNB-type CHF was identified by a sudden rise in surface temperature and the formation of a vapor blanket on the upper heated surface due to asymmetric temperature distribution. The CHF increased due to the sweeping effect of bubbles generated on the heated surface as liquid inertia increased, indicating that maintaining high mass flux can help prevent CHF and enhance system safety. Katto and Ohno's correlation [18] was found to predict CHF most accurately.

These findings underscore the importance of subcooled flow boiling in enhancing thermal management for future EV charging systems, and other industrial applications, such as nuclear reactor cooling systems, where concentric annuli are used. Further research is needed to consider conditions where the actual charging cable may not remain horizontal but could be vertical, angled, or bent. Analyzing the impact of various installation conditions on heat transfer and critical heat flux will contribute to developing more practical and reliable thermal management solutions for EV charging cables.

Table 9
Assumptions used for predicting EV charging time from laboratory-scale experiments.

Assumptions	Remarks
Cable length	Estimations are based on a laboratory test model with a length of 30 cm. The laboratory results are limited by this cable length, which is significantly shorter than the actual charging cables that are over 3 m long. As the cable length increases, insufficient maintenance of inlet subcooling could lead to dry out, reduced heat transfer coefficients, and the risk of system burnout due to reaching CHF.
Heat generation	The experiment did not test the actual charging cable with Joule heating, but used a cartridge heater that accounts for 80 °C copper resistivity and temperature coefficient. Real cables consist of thin, twisted strands, which could result in different heat transfer characteristics compared to the solid cartridge heater used in the experiment.
Concentricity	Assumes perfect concentricity is maintained throughout the cable. Maintaining such concentricity is challenging in reality, and additional structures may need to be installed at intervals along the cable, which could weaken heat transfer and increase flow resistance.
Flow direction	The experiment tested only horizontal flow, but in real-world scenarios, charging cables may be positioned vertically, at angles, or in bent shapes, which could significantly alter heat transfer and critical heat flux.
Charging power consistency	Maximum possible continuous charging conditions without variations in charging power. In real-world scenarios, the charging rate varies significantly depending on the state of the battery. When the battery is nearly discharged, the charging speed is fast, but as it approaches full charge, the charging power decreases sharply to ensure safety.

Note: Readers are advised to carefully consider the assumptions used in this analysis and exercise caution when comparing cooling performance. The values presented in Fig. 15 are estimated based on the specified assumptions.

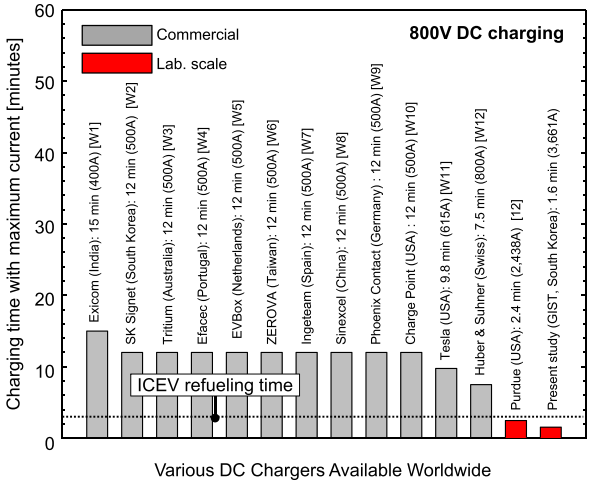

Fig. 15. Time taken for 80 % charging of a 100 kWh EV battery using the continuous charging method with various DC chargers available worldwide. The achievable charging time demonstrated by a previous study with a 304.8 mm long horizontal concentric annulus at a maximum heat flux of $q''_s = 199{,}210$ W/m^2 and a charging current of $I_{wire} = 2438$ A is noted. Also, the achievable charging time, as determined by the current experimental study using a 300 mm long horizontal concentric annulus at a maximum heat flux of $q''_s = 460{,}000$ W/m^2 and a charging current of $I_{wire} = 3661$ A, is provided as a reference.

CRediT authorship contribution statement

Haein Jung: Writing – original draft, Methodology, Investigation, Data curation. **Seunghyun Lee:** Writing – review & editing, Writing – original draft, Supervision, Funding acquisition, Conceptualization.

Declaration of generative AI and AI-assisted technologies in the writing process

During the preparation of this work the authors used large language model (ChatGPT 3.5) in order to proofread and correct grammatical errors in the writings. After using this tool/service, the authors reviewed and edited the content as needed and take full responsibility for the content of the publication.

Declaration of competing interest

The authors declare that they have no known competing financial interests or personal relationships that could have appeared to influence the work reported in this paper.

Data availability

Data will be made available on request.

Acknowledgement

The authors are grateful for the support of the Korea Electric Power Corporation (Grant number: R20XO02-32) and the National Research Foundation of Korea (NRF) grant funded by the Ministry of Science and ICT (MSIT) of Korea government (NRF-RS-2023-00280898).

Appendix A. Supplementary data

Supplementary data to this article can be found online at https://doi.org/10.1016/j.csite.2024.105122.

References

[1] H. Alimoradi, M. Shams, N. Ashgriz, A. Bozorgnezhad, A novel scheme for simulating the effect of microstructure surface roughness on the heat transfer characteristics of subcooled flow boiling, Case Stud, Therm. Eng. 24 (2021) 100829.
[2] A. Bozorgnezhad, M. Shams, G. Ahmadi, H. Kanani, M. Hasheminasab, The experimental study of water accumulation in PEMFC cathode channel, in: Fluids Engineering Division Summer Meeting, vol. 57212, American Society of Mechanical Engineers, 2015. July. V001T22A004.
[3] M. Hasheminasab, A. Bozorgnezhad, M. Shams, G. Ahmadi, H. Kanani, Simultaneous investigation of PEMFC performance and water content at different flow rates and relative humidities, in: International Conference on Nanochannels, Microchannels, and Minichannels, vol. 46278, American Society of Mechanical Engineers, 2014. August. V001T07A002.
[4] A. Bozorgnezhad, M. Shams, H. Kanani, M. Hasheminasab, Experimental investigation on dispersion of water droplets in the single-serpentine channel of a PEM fuel cell, J. Dispersion Sci. Technol. 36 (8) (2015) 1190–1197.
[5] M. Ashrafi, M. Shams, A. Bozorgnezhad, G. Ahmadi, Simulation and experimental validation of droplet dynamics in microchannels of PEM fuel cells, Heat Mass Tran. 52 (2016) 2671–2686.
[6] H. Kanani, M. Shams, M. Hasheminasab, A. Bozorgnezhad, Model development and optimization of operating conditions to maximize PEMFC performance by response surface methodology, Energy Convers. Manag. 93 (2015) 9–22.
[7] A. Bozorgnezhad, M. Shams, H. Kanani, M. Hasheminasab, G. Ahmadi, Two-phase flow and droplet behavior in microchannels of PEM fuel cell, Int. J. Hydrogen Energy 41 (42) (2016) 19164–19181.
[8] A. Bozorgnezhad, M. Shams, H. Kanani, M. Hasheminasab, G. Ahmadi, The experimental study of water management in the cathode channel of single-serpentine transparent proton exchange membrane fuel cell by direct visualization, Int. J. Hydrogen Energy 40 (6) (2015) 2808–2832.
[9] L. Chapman, Transport and climate change: a review, J. Transport Geogr. 15 (2007) 354–367.
[10] D. Mitchell, M.R. Allen, J.W. Hall, B. Muller, L. Rajamani, C.L. Quéré, The myriad challenges of the Paris Agreement, Philos. Trans. R. Soc. A Math. Phys. Eng. Sci. 376 (2018) 20180066.
[11] Y. Wu, H. Yu, J. Zhang, X. Xu, R. Dai, W. Liu, H. Lv, Y. Xu, Q. Wang, H. He, J. Zheng, Optimal design of liquid cooling structures for superfast charging cable cores under a high current load, Case Stud. Therm. Eng. 53 (2024) 103821.
[12] V.S. Devahdhanush, S. Lee, I. Mudawar, Experimental investigation of subcooled flow boiling in annuli with reference to thermal management of ultra-fast electric vehicle charging cables, Int. J. Heat Mass Tran. 172 (2021) 121176.
[13] Y. Lee, Turbulent heat transfer from the core tube in thermal entrance regions of concentric annuli, Int. J. Heat Mass Tran. 11 (46) (1968) 509–522.
[14] J.H. Lim, H. Oh, S.W. Lee, M. Park, S. Lee, H. Jo, A novel integrated PDB-FDB model for the prediction of flow boiling heat transfer under high sub-cooling and very high heat flux conditions, Int. J. Heat Mass Tran. 208 (2023).
[15] J.G. Collier, J.R. Thome, Convective Boiling and Condensation, Clarendon Press, 1994.
[16] D.D. Hall, I. Mudawar, Critical heat flux (CHF) for water flow in tubes-II. Subcooled CHF correlations, Int. J. Heat Mass Tran. 43 (14) (2000) 2605–2640.
[17] K.M. Becker, D. Djursing, K. Lindberg, O. Eklind, C. Österdahl, Burnout conditions for round tubes at elevated pressures, in: Proc. Int. Symp. Two-phase Syst, Elsevier, 1972, pp. 55–73.
[18] Y. Katto, H. Ohno, An improved version of the generalized correlation of critical heat flux for the forced convective boiling in uniformly heated vertical tubes, Int. J. Heat Mass Tran. 27 (1984) 1641–1648.
[19] M. Shah, Improved general correlation for critical heat flux during upflow in uniformly heated vertical tubes, Int. J. Heat Fluid Flow 8 (1987) 326–335.
[20] P.K. Sarma, V. Srinivas, K.V. Sharma, V.D. Rao, G.P. Celata, A correlation to evaluate critical heat flux in small diameter tubes under subcooled conditions of the coolant, Int. J. Heat Mass Tran. 49 (1–2) (2006) 42–51.
[21] K. Hata, M. Shiotsu, N. Noda, Critical heat flux of subcooled water flow boiling for high L/d region, Nucl. Sci. Eng. 154 (1) (2006) 94–109.
[22] V. Ganesan, R. Patel, J. Hartwig, I. Mudawar, Universal critical heat flux (CHF) correlations for cryogenic flow boiling in uniformly heated tubes, Int. J. Heat Mass Tran. 166 (2021) 120678.
[23] H. Zhang, I. Mudawar, M.M. Hasan, Photographic study of high-flux subcooled flow boiling and critical heat flux, Int. Commun. Heat Mass Tran. 34 (2007) 653–660.
[24] C.R. Kharangate, I. Mudawar, M.M. Hasan, Photographic study and modeling of critical heat flux in horizontal flow boiling with inlet vapor void, Int. J. Heat Mass Tran. 55 (2012) 4154–4168.
[25] J. Lee, I. Mudawar, Critical heat flux for subcooled flow boiling in micro-channel heat sinks, Int. J. Heat Mass Tran. 52 (13) (2009) 3341–3352.
[26] R.L. Judd, J.H.T. Wade, Forced Convection Heat Transfer in Eccentric Annular Passages, Heat Transfer and Fluid Mechanics Institute, Stanford University Press, 1963, pp. 272–288.
[27] E.Y. Leung, W.M. Kays, W.C. Reynolds, Heat Transfer with Turbulent Flow in Concentric and Eccentric Annuli with Constant and Variable Heat Flux, Report No. AHT-4, Stanford University, California, 1961.
[28] Y. Lee, H. Barrow, Paper 12: turbulent flow and heat transfer in concentric and eccentric annuli, in: Proc. Inst. Mech. Engr., SAGE Publications Sage, London, UK, 1963, pp. 1–16.
[29] S.J. Kline, The purposes of uncertainty analysis, J. Fluid Eng. 107 (1985) 153–160.
[30] R.J. Moffat, Describing the uncertainties in experimental results, Exp. Therm. Fluid Sci. 1 (1988) 3–17.
[31] R.W. Hanks, The laminar-turbulent transition for flow in pipes, concentric annuli, and parallel plates, AIChE J. 9 (1) (1963) 45–48.
[32] O.C. Jones, J.C.M. Leung, An improvement in the calculation of turbulent friction in smooth concentric annuli, J. Fluid Eng. 103 (4) (1981) 615–623.
[33] W. Zhi-qing, Study on correction coefficients of laminar and turbulent entrance region effect in round pipe, Appl. Math. Mech. 3 (1982) 433–446.
[34] V.S. Devahdhanush, S. Lee, I. Mudawar, Consolidated theoretical/empirical predictive method for subcooled flow boiling in annuli with reference to thermal management of ultra-fast electric vehicle charging cables, Int. J. Heat Mass Tran. 175 (2021) 121224.
[35] M. Al-Arabi, Turbulent heat transfer in the entrance region of a tube, Heat Tran. Eng. 3 (3–4) (1982) 76–83.
[36] W.M. Kays, E.Y. Leung, Heat transfer in annular passages—hydrodynamically developed turbulent flow with arbitrarily prescribed heat flux, Int. J. Heat Mass Tran. 6 (7) (1963) 537–557.
[37] T. Sato, H. Matsumura, On the conditions of incipient subcooled-boiling with forced convection, Bull. JSME 7 (26) (1964) 392–398.
[38] F.W. Dittus, L.M.K. Boelter, Heat transfer in automobile radiators of the tubular type, Int. Commun. Heat Mass Tran. 12 (1) (1985) 3–22.
[39] R.H.S. Winterton, Where did the Dittus and Boelter equation come from? Int. J. Heat Mass Tran. 41 (1998) 809–810.

[40] M.M. Shah, A general correlation for heat transfer during subcooled boiling in pipes and annuli, Build. Eng. 83 (1) (1977) 202–217.
[41] C.A. Chen, K.W. Li, T.F. Lin, W.-K. Li, W.-M. Yan, Study on heat transfer and bubble behavior inside horizontal annuli: experimental comparison of R-134a, R–407C, and R-410A subcooled flow boiling, Case Stud. Therm. Eng. 24 (2021).
[42] G. Yang, W. Zhang, M. Binama, J. Sun, W. Cai, Review on bubble dynamic of subcooled flow boiling-part a: research methodologies, Int. J. Therm. Sci. 184 (2023) 108019.
[43] Y.Y. Hsu, R.W. Graham, Transport Processes in Boiling and Two-phase Systems, American Nuc. Soc, Inc., Illinois, USA, 1986.
[44] S.S. Papell, Subcooled Boiling Heat Transfer under Forced Convection in a Heated Tube, NASA Technical Note D-1583, Lewis Research Center, Cleveland, OH, USA, 1963.
[45] M. Badiuzzaman, Correlation of subcooled boiling data, Pakistan Eng. 7 (1967) 759–764.
[46] F.D. Moles, J.F.G. Shaw, Boiling heat transfer to sub-cooled liquids under conditions of forced convection, Trans. Inst. Chem. Eng. 50 (1) (1972) 76–84.
[47] E.N. Sieder, G.E. Tate, Heat transfer and pressure drop of liquids in tubes, Ind. Eng. Chem. 28 (12) (1936) 1429–1435.
[48] M.M. Shah, Generalized prediction of heat transfer during subcooled boiling in annuli, Heat Tran. Eng. 4 (1) (1983) 24–31.
[49] K.E. Gungor, R.H.S. Winterton, A general correlation for flow boiling in tubes and annuli, Int. J. Heat Mass Tran. 29 (3) (1986) 351–358.
[50] Z. Liu, R.H.S. Winterton, A general correlation for saturated and subcooled flow boiling in tubes and annuli, based on a nucleate pool boiling equation, Int. J. Heat Mass Tran. 34 (11) (1991) 2759–2766.
[51] M.M. Shah, New correlation for heat transfer during subcooled boiling in plain channels and annuli, Int. J. Therm. Sci. 112 (2017) 358–370.
[52] K. Cornwell, J.G. Einarsson, Influence of fluid flow on nucleate boiling from a tube, Exp. Heat Transf, Int. J. 3 (2) (1990) 101–116.
[53] J. Shaw, Subcooled Boiling Heat Transfer to Liquids under Conditions of Forced Convection, PhD Thesis, Chemical Engineering, University of Surrey, Guildford, Surrey, UK, 1972.
[54] K. Hata, M. Shiatzu, N. Noda, Critical heat fluxes of subcooled water flow boiling against outlet subcooling in short vertical tube, J. Heat Tran. 126 (3) (2004) 312–320.

Web references

[W1] https://www.exicom-ps.com/business-solutions.
[W2] https://sksignet.us/distributed/400kw-dp–600kw-pc.
[W3] https://tritiumcharging.com/product/pk-350/.
[W4] https://electricmobility.efacec.com/high-power-ultra-fast-charging-station-350-kw/.
[W5] https://evbox.com/en/ev-chargers/troniq-high-power.
[W6] https://www.zerovatech.com/product/dq-series-480kw-standalone-fast-charger/.
[W7] https://www.ingeteam.com/Portals/0/Catalogo/Producto/Documento/PRD_4248_Archivo_ingeteam-rapidst-en.pdf.
[W8] https://en.sinexcel.com/evcharger/360-480kw.php.
[W9] https://www.phoenixcontact.com/en-au/products/charging-technology-for-e-mobility/dc-charging-cables#ex-content-transclusion-snippet–242.
[W10] https://www.chargepoint.com/businesses/dc-stations/express-plus.
[W11] https://electrek.co/2023/03/15/tesla-supercharger-v4-revealed-twice-as-powerful/.
[W12] https://www.hubersuhner.com/en/markets/industry/ev-charging-infrastructure/ev-fast-charging/high-power-charging-hpc.